Linear Parameter-Varying Polytopic Modeling and Control Design for Guided Projectiles

Vinco, Gian Marco; Sename, Olivier; Strub, Guillaume; Theodoulis, Spilios

DOI
10.2514/1.G007726

Publication date
2024

Document Version
Final published version

Published in
Journal of Guidance, Control, and Dynamics

Citation (APA)
Vinco, G. M., Sename, O., Strub, G., & Theodoulis, S. (2024). Linear Parameter-Varying Polytopic Modeling and Control Design for Guided Projectiles. *Journal of Guidance, Control, and Dynamics*, *47*(3), 433-447. https://doi.org/10.2514/1.G007726

JOURNAL OF GUIDANCE, CONTROL, AND DYNAMICS
Vol. 47, No. 3, March 2024

Linear Parameter-Varying Polytopic Modeling and Control Design for Guided Projectiles

Gian Marco Vinco* and Olivier Sename†
University Grenoble Alpes, 38000 Grenoble, France
Guillaume Strub‡
French-German Research Institute of Saint-Louis, 68300 Saint-Louis, France
and
Spilios Theodoulis§
Delft University of Technology, 2629 HS Delft, The Netherlands

https://doi.org/10.2514/1.G007726

In this paper, a linear parameter varying (LPV) modeling and control design approach is applied to a new class of guided projectiles, aiming to exploit the advantages of the LPV framework in terms of guaranteed stability and performance. The investigated concept consists of a planar symmetric 155 mm fin-stabilized projectile equipped with a reduced amount of control actuators and characterized by a predominantly unstable behavior across the analyzed flight envelope. A dedicated modeling procedure allows reformulating the nonlinear projectile dynamics as a LPV polytopic system, employed for the controller design. The procedure intends to reduce the computational complexity and the conservativeness affecting the overall controller synthesis. A trajectory-tracking simulation scenario is performed in a realistic simulator environment to assess the performance of the resulting LPV polytopic autopilot across the entire flight envelope.

I. Introduction

IN THE last few decades, the Linear Parameter Varying (LPV) framework has attracted increasing interest in the modeling and control of a wide range of aerospace applications. Initial studies presented the LPV modeling approach as a perfect match for the well-established gain-scheduling controller design technique, leading to relevant contributions concerning missile [1–5] and aircraft [6–8] applications. Several studies have also focused the investigation on guided projectiles, intending to improve the accuracy and range capability of artillery operations. LPV modeling has been coupled with robust control design for spin-stabilized [9–11] and fin-stabilized [12,13] projectiles' architectures. However, the LPV models were generally obtained as a collection of local linearizations of the original nonlinear dynamics, leading to the possible loss of important information regarding the system's transient behavior. The gain-scheduled autopilots result from interpolating the corresponding set of linear time-invariant (LTI) controllers, designed at the trimming conditions selected during the model linearization. Consequently, fundamental properties such as stability and flight performances are guaranteed only about the analyzed trimming points and not at all the remaining flight conditions [14,15].

These limitations motivated the investigation of alternative LPV-based design approaches, providing a better representation of the overall system dynamics [16–18] and robustness and performance properties across the entire flight envelope [19–22]. Concerning guided projectiles, only recently, a LPV approach has been developed in the framework of Model Predictive Control [23], opening several opportunities for further investigations. The LPV design discussed in the present paper relies on the polytopic formulation. First introduced in [24], the polytopic approach allows the synthesis of a controller that guarantees stability and performance for any conditions of the varying parameters in a selected convex subset (polytope), defined by the ranges of variation of each parameter. In particular, the polytopic control design only targets the operating conditions characterizing the vertices of the selected convex subset, resulting in a significantly limited number of local controllers being interpolated (one per vertex), and reducing the computational complexity at the implementation stage. However, it requires a nontrivial affine model-parameters relation characterizing the system, and the overall optimization process can be affected by an excessive level of conservatism that can deteriorate the performance of the controller. Thus, several studies have focused on the optimization of the polytope's dimension [generally two-dimensional (2D) convex spaces] and the consistency of the operating conditions belonging to the convex subset [25–32].

This paper proposes a LPV $\mathcal{H}_\infty$ controller design for the pitch channel dynamics of a new class of long range guided projectiles. Interesting properties of the analyzed concept derive from selecting a reduced set of control actuators, leading to a noncoplanar canards/fins configuration [33,34] and a predominant statically unstable behavior. During the ballistic ascending phase of the trajectory, the canards are folded in the sabot, and the projectile is characterized by a tetragonally symmetric body and a stable configuration. After reaching the apogee, a set of two canards is deployed along the horizontal plane of the projectile, reducing the symmetry of the body from tetragonal to planar during the gliding phase of the trajectory. In this configuration, the aerodynamic contributions generated by the canards have a destabilizing effect on the projectile dynamics. The design of a statically unstable configuration aims to improve the maneuverability of the projectile, compensating for the limited control authority caused by the reduced number of control surfaces. Recent research on long-range guided projectiles [35] underlined the impact of the canards/fins configuration, aerodynamics modeling, and guidance development on the overall range capability. In a previous study [36], the full

Presented as Paper 2023-2498 at the 2023 AIAA Science and Technology Forum and Exposition (SciTech Forum), National Harbor, Maryland, US, January 23–27, 2023; received 17 May 2023; accepted for publication 14 October 2023; published online 25 January 2024.

*Ph.D. Student, CNRS, Grenoble INP, GIPSA-Lab, 11 rue des Mathématiques, 38402, Saint Martin d'Hères, France; also Guidance Navigation & Control Department, French-German Research Institute of Saint-Louis, Saint-Louis, 68300, France; Gian-Marco.Vinco@grenoble-inp.fr. Student Member AIAA.

†Professor, CNRS, Grenoble INP, GIPSA-Lab, 11 rue des Mathématiques, 38402, Saint Martin d'Hères, France; Olivier.Sename@grenoble-inp.fr.

‡Researcher Scientist, Guidance Navigation & Control Department, 5 rue du Général Cassagnou; Guillaume.Strub@isl.eu.

§Associate Professor, Control & Simulation Section, Control & Operations Department, Faculty of Aerospace Engineering, Kluyverweg 1; Spilios.Theodoulis@isl.eu. Associate Fellow AIAA.

nonlinear dynamics of the projectile was derived and converted into a corresponding quasi-LPV model through the state transformation technique [37], trying to minimize the need for model approximations. The main contribution of the present work relies on the development of a control-oriented modeling procedure, which 1) reformulates the quasi-LPV model of the projectile to comply with the requirements of polytopic systems and 2) optimizes the dimension of the obtained polytope to reduce the conservativeness of the controller synthesis.

In particular, the optimization analysis is applied on a three-dimensional (3D) polytope which represents all the possible flight conditions that can occur during the trajectory of the projectile. The results of the control design are tested in a simulator environment through a trajectory tracking scenario where a preliminary ad hoc implemented guidance law targets the optimization of the aerodynamic lift-to-drag ratio during the gliding phase of the trajectory [38,39].

The paper is divided as follows. The nonlinear dynamics of the guided projectile is first discussed in Sec. II, along with the derivation of the corresponding quasi-LPV model. In Sec. III, the theoretical formulation of the LPV polytopic class of systems is presented. A complete approximation analysis allows reformulating the obtained quasi-LPV model to satisfy the polytopic requirements. Once the accuracy of the approximations is verified, the dimensions of the investigated flight envelope are optimized to reduce the complexity of the controller synthesis process. Later, Sec. IV details the generalized scheme employed for the synthesis of a LPV polytopic controller based on $\mathcal{H}_\infty$ design. Then, the results of the controller design are evaluated in the frequency domain. Finally, Sec. V proposes a reference tracking simulation scenario, employing the LPV polytopic controller to target an angle-of-attack guidance trajectory. The ultimate purpose is to prove the capability of the LPV design to ensure competitive performances and stability properties across all the conditions described by the selected flight envelope.

II. Projectile Pitch Channel Dynamics

This section describes the projectile's physical concept, design properties, and operational objectives. The nonlinear model representing the pitch channel dynamics is discussed, including some relevant insights concerning the aerodynamic characterization and the allocation of the control input. Later, the nonlinear model is converted into a corresponding quasi-LPV one using the State Transformation technique. The obtained quasi-LPV model will be reformulated as a polytopic system in the next section and employed for the robust controller design.

A. Nonlinear Model

The investigated nonlinear model refers to a 155 mm fin-stabilized guided projectile, characterized by a set of two front control canards and a set of four symmetrical rear fins, noncoplanar to the plane of symmetry of the canards, as shown in Fig. 1a. The reduced amount of control surfaces limits the resulting control authority but is justified by the intention of improving the projectile operating range through a bank-to-turn (BTT) flight strategy, employed during the gliding phase of the trajectory, as shown in Fig. 1b.

The full six-degrees-of-freedom (DoF) nonlinear model of the projectile was derived in a previous study [36], including an extensive characterization of the aerodynamic contributions. The results of the analysis led to the development of the simulator environment employed in the last session of the present article for the autopilot performance assessment. The interested reader can find an overview of the six-DoF projectile dynamics in Appendix A. For the interest of this study, the analysis focuses on the pitch channel only, consisting of the dynamics of the aerodynamic angle-of-attack (AoA) α, and of the pitch rate q, expressed with respect to the system of coordinates integral to the projectile's body:

$$\begin{aligned}\dot{\alpha} &= -\frac{X\sin\alpha}{mV\cos\beta} + \frac{Z\cos\alpha}{mV\cos\beta} + \frac{g}{V\cos\beta}(\sin\alpha\sin\theta + \cos\alpha\cos\theta\cos\phi)\\ &\quad + q - p\tan\beta\cos\alpha - r\tan\beta\sin\alpha;\\ \dot{q} &= \frac{1}{I_{yy}}[M - pr(I_{xx} - I_{zz})]\end{aligned} \tag{1}$$

The lateral contributions of the yaw rate and the aerodynamic angle-of-sideslip (AoS), r and β, respectively, as well as the influence of the roll angle and the roll rate, ϕ and p, respectively, are assumed to be negligible for the pitch channel dynamics. Indeed, the AoS minimization (BTT) strategy, together with the particular geometry of the concept, allows the decoupling of the projectile dynamics between its lateral and pitch axes. The pitch angle θ is not accounted for as a parameter of the LPV analysis, so a nominal value was selected based on a set of preliminary simulation tests. The term V represents the true airspeed in zero relative wind conditions.

In terms of physical parameters, I_{xx}, I_{yy}, and I_{zz} correspond to the moments of inertia relative to the principal axes of the projectile's body; m stands for the overall mass; and g stands for the standard acceleration of gravity, under flat Earth assumptions. Because of the characteristic second-order rotational symmetry of the projectile's body, the off-diagonal inertial coupling terms, I_{xy}, I_{yz}, and I_{xz}, present in the inertia matrix, are neglected as well.

Additionally, the pitch channel dynamics is highly affected by the aerodynamic contributions, in the form of longitudinal and vertical forces, X and Z, respectively, and pitching moment M modeled through an extensive regression analysis based on a set of computational fluid dynamics (CFD) data, as follows:

$$\begin{aligned}X &= \bar{q}S(C_{X_{\alpha_0}} + C_{X_{\alpha_2}}\sin^2\alpha + C_{X_{\alpha_4}}\sin^4\alpha + C_{X_{\delta_0}} + C_{X_{\delta_2}}\sin^2\delta_{\text{eff}});\\ Z &= \bar{q}S\left[C_{Z_{\alpha_1}}\sin\alpha + \left(\frac{d}{2V}\right)C_{Z_q}q + C_{Z_{\delta_1}}\sin\delta_q + C_{Z_{\delta_3}}\sin^3\delta_q\right];\\ M &= \bar{q}Sd\left[C_{m_{\alpha_1}}\sin\alpha + C_{m_{\alpha_3}}\sin^3\alpha + C_{m_{\alpha_5}}\sin^5\alpha + \left(\frac{d}{2V}\right)C_{m_q}q\right.\\ &\quad \left. + C_{m_{\delta_1}}\sin\delta_q + C_{m_{\delta_3}}\sin^3\delta_q\right]\end{aligned} \tag{2}$$

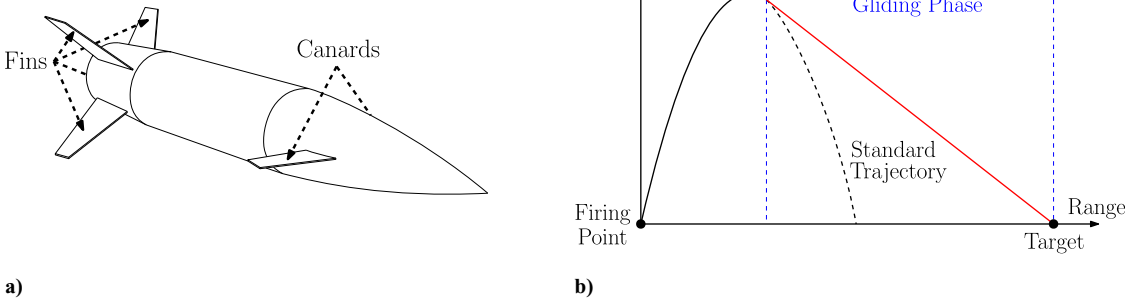

a) b)

Fig. 1 Long-range guided projectile: a) projectile concept and b) range enhancement flight strategy.

The aerodynamic model is defined by the set of aerodynamic regression coefficients related to the longitudinal static ($C_{X_{\alpha_0}}$, $C_{X_{\alpha_2}}$, $C_{X_{\alpha_4}}$) and control ($C_{X_{\delta_0}}$, $C_{X_{\delta_2}}$) forces; to the vertical static ($C_{Z_{\alpha_1}}$), damping (C_{Z_q}), and control ($C_{Z_{\delta_1}}$, $C_{Z_{\delta_3}}$) forces; and finally to the pitching static ($C_{m_{\alpha_1}}$, $C_{m_{\alpha_3}}$, $C_{m_{\alpha_5}}$), damping (C_{m_q}), and control ($C_{m_{\delta_1}}$, $C_{m_{\delta_3}}$) moments. Each of the previous aerodynamic coefficients has been obtained as a function of a selected range of subsonic Mach values $\mathcal{M}$. Additionally, the aerodynamic model depends on the values of the projectile's reference surface S and caliber d and on the dynamic pressure $\bar{q}$, which is defined as a nonlinear function of the altitude h through the air density variation. The full aerodynamic model is provided in Appendix B.

Furthermore, the local deflection angles characterizing the right and the left control canards δ_r and δ_l, respectively, are allocated into a set of virtual deflections. The virtual deflections express the control action in terms of a roll contribution δ_p and a pitch contribution δ_q obtained, respectively, through a differential or a concurrent deflection of the individual surfaces, following the static allocation strategy:

$$\begin{bmatrix} \delta_p \\ \delta_q \end{bmatrix} = \begin{bmatrix} -\frac{1}{2} & +\frac{1}{2} \\ +\frac{1}{2} & +\frac{1}{2} \end{bmatrix} \begin{bmatrix} \delta_r \\ \delta_l \end{bmatrix} \tag{3}$$

The longitudinal control contribution, $\delta_{\text{eff}} = \sqrt{\delta_p^2 + \delta_q^2}$, has been modeled as a nonlinear combination of the virtual roll and pitch deflections. It represents a braking effect due to the additional drag generated by the canard deflections.

B. Quasi-LPV Model

The nonlinear dynamics in Eqs. (1–3) can be reformulated more compactly as an output nonlinear system [1]. However, this formulation requires the system to be affine in the input; thus, a first-order approximation of the aerodynamic control coefficients ($C_{Z_{\delta_1}}$, $C_{Z_{\delta_3}}$, $C_{m_{\delta_1}}$, $C_{m_{\delta_3}}$) was investigated in detail in [37] and applied to the pitch channel dynamics. The resulting nonlinear *Simplified* model is used for the LPV modeling and control design, accounting for the aerodynamic approximations as a source of uncertainties to be handled by the controller. The remaining nonlinear contributions characterizing the model are functions of the set of continuous time-varying parameters $\rho(t)$. They can be collected in the generalized terms, $f_1(\rho)$ and $f_2(\rho)$, as:

$$\begin{bmatrix} \dot{\alpha} \\ \dot{q} \end{bmatrix} = \begin{bmatrix} f_1(\rho) \\ f_2(\rho) \end{bmatrix} + \begin{bmatrix} 0 & A_{12}(\rho) \\ 0 & A_{22}(\rho) \end{bmatrix} \begin{bmatrix} \alpha \\ q \end{bmatrix} + \begin{bmatrix} B_1(\rho) \\ B_2(\rho) \end{bmatrix} \delta_q;$$
$$\rho(t) = [\alpha(t), V(t), h(t)] \tag{4}$$

where:

$$A_{12}(\rho) = 1 + \frac{\bar{q}SdC_{Z_q}\cos\alpha}{2mV^2}; \qquad B_1(\rho) = \frac{\bar{q}SC_{Z_{\delta_1}}\cos\alpha}{mV};$$
$$A_{22}(\rho) = \frac{\bar{q}Sd^2C_{m_q}}{2I_{yy}V}; \qquad B_2(\rho) = \frac{\bar{q}SdC_{m_{\delta_1}}}{I_{yy}} \tag{5}$$

Starting from the output nonlinear *Simplified* pitch channel dynamics in Eqs. (4) and (5), a reliable quasi-LPV model is obtained by employing the systematic State Transformation technique [1,2]. The complete derivation of the LPV model from the nonlinear *Simplified* one is detailed in [37]. Despite being restricted to a limited class of systems, the State Transformation approach provides a quasi-LPV model that corresponds to an exact transformation of the original nonlinear system, avoiding any additional forms of approximation. In particular, it aims to hide the nonlinear parameter-varying terms, $f_1(\rho)$ and $f_2(\rho)$, present in the model through a redefinition of the nonscheduling state and the input variables of the system, respectively, q and δ_q in Eq. (4). The new state vector of the quasi-LPV pitch channel dynamics model includes the AoA and the off-equilibrium value of the pitch rate q_{dev} defined during the transformation process, as in Eq. (6). Accordingly, the off-equilibrium value of the virtual pitch deflection input $\delta_{q,\text{dev}}$ is expressed as

$$q_{\text{dev}} \coloneqq q - q_{\text{eq}}(\rho); \qquad \delta_{q,\text{dev}} \coloneqq \delta_q - \delta_{q,\text{eq}}(\rho) \tag{6}$$

where the equilibrium functions $q_{\text{eq}}(\rho)$ and $\delta_{q,\text{eq}}(\rho)$ are obtained by trimming the pitch channel dynamics of the projectile in Eqs. (4) and (5) across the entire flight envelope described by the variation of the scheduling vector $\rho(t)$. An overview of the transformation procedure is given in Appendix C. The dynamics of the off-equilibrium variables $\dot{q}_{\text{dev}}$ and $\dot{\delta}_{q,\text{dev}}$ are expressed through the derivatives of the corresponding equilibrium functions $q_{\text{eq}}(\rho)$ and $\delta_{q,\text{eq}}(\rho)$, respectively.

Finally, the inclusion of an integrator at the input of the system defines the new input $\delta_q = \int\sigma$. This solution allows removing the dependence of the input from the current equilibrium flight conditions, which was introduced by the transformation process and can strongly affect the stability of the system [17]. Additionally, the integration redefines the input matrix B of the quasi-LPV system in a parameter-independent form. The latter observation represents a fundamental requirement for the later LPV control design. From a modeling perspective, the presence of the integrator can be justified by assuming that the controller intended to be developed accounts for a pure integral action, formally included in the system definition.

The resulting integrator *Augmented* quasi-LPV model of the projectile pitch channel dynamics corresponds to:

$$\begin{bmatrix} \dot{\alpha} \\ \dot{q}_{\text{dev}} \\ \dot{\delta}_{q,\text{dev}} \end{bmatrix} = \begin{bmatrix} 0 & A_{12}(\rho) & B_1(\rho) \\ 0 & \tilde{A}_{22}(\rho) & \tilde{B}_2(\rho) \\ 0 & \tilde{A}_{32}(\rho) & \tilde{B}_3(\rho) \end{bmatrix} \begin{bmatrix} \alpha \\ q_{\text{dev}} \\ \delta_{q,\text{dev}} \end{bmatrix} + \begin{bmatrix} 0 \\ 0 \\ 1 \end{bmatrix} \sigma;$$
$$\rho(t) = [\alpha(t), V(t), h(t)] \tag{7}$$

with:

$$\tilde{A}_{22}(\rho) := A_{22}(\rho) - \frac{\partial q_{\text{eq}}}{\partial\alpha}A_{12}(\rho); \quad \tilde{B}_2(\rho) := B_2(\rho) - \frac{\partial q_{\text{eq}}}{\partial\alpha}B_1(\rho);$$
$$\tilde{A}_{32}(\rho) := -\frac{\partial\delta_{q,\text{eq}}}{\partial\alpha}A_{12}(\rho); \qquad \tilde{B}_3(\rho) := -\frac{\partial\delta_{q,\text{eq}}}{\partial\alpha}B_1(\rho) \tag{8}$$

III. From Quasi-LPV to Polytopic Formulation

In this section, the *Augmented* quasi-LPV model of the projectile in Eqs. (7) and (8) is reformulated as a polytopic system, for the later control design. The main theoretical features and requirements of the polytopic class of systems are first discussed to verify which aspects of the obtained quasi-LPV model must be adjusted to comply with the polytopic formulation. Later, an extensive model-parameter dependence analysis allows for an accurate approximation of the quasi-LPV model, by mapping the original set of scheduling variables into a new set of scheduling functions that respect the polytopic requirements. Finally, the dimensions of the polytope defined by the new set of scheduling functions are investigated to minimize the conservatism and the computational complexity affecting the following controller synthesis.

A. LPV Polytopic Background

The polytopic formulation proposed here is based on [24], complying with the same notation. As previously mentioned, this approach is restricted to a class of LPV systems characterized by an affine dependence on the selected set of time-varying scheduling variables. This implies the system is linear with respect to each entry of $\rho(t) = [\rho_1, \ldots, \rho_{n_\rho}]$. Additionally, the system must be input- and output-parameter independent to satisfy the affine conditions. The latter restriction can be generally relaxed by prefiltering

the input and the output. Finally, measurements of the scheduling variables are supposed to be available in real time, while their variation is assumed bounded between a minimum and a maximum value:

$$\underline{\rho_j} \leq \rho_j \leq \overline{\rho_j}$$

where $j \in [1, n_\rho]$ and $\overline{\rho_j}$ and $\underline{\rho_j}$ indicate the upper and lower bounds, respectively, of the jth scheduling variable. The boundary values of the scheduling variables define a convex subspace (polytope) of 2^{n_ρ} vertices, $\omega = [\omega_1, \ldots, \omega_{2^{n_\rho}}]$. At each vertex, $\omega_i = [\nu_{i1}, \ldots, \nu_{in_\rho}]$ with $i \in [1, 2^{n_\rho}]$, the jth scheduling variable, ν_{ij}, equals either $\overline{\rho_j}$ or $\underline{\rho_j}$. The corresponding set of LTI realizations of the system, evaluated at each vertex of the polytope, allows obtaining a general representation of the LPV system as the following convex interpolation:

$$\begin{bmatrix} A(\rho) & B(\rho) \\ C(\rho) & D(\rho) \end{bmatrix} = \sum_{i=1}^{2^{n_\rho}} \mu_i \begin{bmatrix} A(\omega_i) & B(\omega_i) \\ C(\omega_i) & D(\omega_i) \end{bmatrix} \tag{9}$$

The interpolation function $\mu_i(\rho)$ is computed for each vertex as:

$$\mu_i(\rho) = \frac{\prod_{j=1}^{n_\rho} |\rho_j - C^c(\omega_i)_j|}{\prod_{j=1}^{n_\rho} (\overline{\rho_j} - \underline{\rho_j})} > 0; \qquad \sum_{i=1}^{2^{n_\rho}} \mu_i(\rho) = 1 \tag{10}$$

where $C^c(\omega_i)_j$ indicates the j^{th} element of the vector $C^c(\omega_i)$, as follows:

$$C^c(\omega_i)_j = \begin{cases} \overline{\rho_j} & \text{if } \omega_i = \underline{\rho_j} \\ \underline{\rho_j} & \text{otherwise} \end{cases}$$

B. Projectile Polytopic Modeling Process

The last modeling step, before the control design, consists of the reformulation of the projectile *Augmented* quasi-LPV model in Eqs. (7) and (8) as the generalized polytopic system in Eq. (9). Through the inclusion of the integrator, the input matrix, $B = [0, 0, 1]^{\mathrm{T}} \in \mathbb{R}^{3x1}$, and the output matrix, $C = I \in \mathbb{R}^{3x3}$, of Eq. (7) are constant parameter independent, while the feedthrough matrix $D = 0$. Additionally, from the scheduling vector in Eq. (7), $n_\rho = 3$. Thus, the projectile polytopic model is obtained as the convex interpolation of the $2^{n_\rho} = 8$ local LTI realizations of the system evaluated at the vertices of the polytope, as in Eqs. (9) and (10). However, the *Augmented* quasi-LPV model in Eqs. (7) and (8) is still nonaffine with respect to the selected set of scheduling variables, $\rho(t) = [\alpha(t), V(t), h(t)]$. Indeed, the entries of the state matrix A in Eq. (5) show an explicit nonlinear dependence on α and V and an implicit nonlinear dependence on h, through the definition of the dynamic pressure $\bar{q}(h)$. Thus, the quasi-LPV model cannot be directly reformulated as a polytopic system. A possible solution consists of mapping $\rho(t)$ into a new set of scheduling functions $\tilde{\rho}(t)$, which satisfies the affine restriction imposed by the polytopic formulation. To this purpose, a model approximation and optimization procedure is developed in the following two main steps:

1) In *model-parameter dependence analysis*, identify a new set $\tilde{\rho}(t)$, characterized by the least necessary number of scheduling functions $n_{\tilde{\rho}}$. Indeed, the computational complexity of the later controller synthesis tends to rapidly increase with $n_{\tilde{\rho}}$ as $\mathcal{O}(2^{n_{\tilde{\rho}}})$.

2) In the *polytope's dimensions reduction*, map the convex space described by the original set $\rho(t)$ into the new one defined by the previously identified set $\tilde{\rho}(t)$. The intention is to minimize the conservativeness of the controller synthesis by optimizing the dimensions of the new polytope.

In the following, the procedure is discussed in detail explaining how each of the steps is applied to the projectile *Augmented* quasi-LPV model.

1. Model-Parameter Dependence Analysis

This analysis intends to reformulate the model in Eqs. (7) and (8) as a polytopic system. The state matrix A is first parameterized in the lowest possible number of scheduling functions, selected based on the following criteria:

1) Favor the selection of nonlinear terms that appear repeatedly in the state matrix.

2) The functions must be affine with the system to comply with the polytopic formulation.

Then, the identified scheduling functions are extensively studied to assess their relevance in the characterization of the system dynamics. Based on the results, each function is either included in the new scheduling vector $\tilde{\rho}(t)$ or neglected. The resulting approximated polytopic model is compared to the original one to estimate the accuracy of the analysis. In the following, the procedure is applied to the projectile quasi-LPV model, subdivided into three main steps.

a. Selection. The nonlinear terms characterizing the state matrix in Eqs. (7) and (8) are selected in accordance with the given criteria and accounted for as possible candidates for the new set $\tilde{\rho}(t)$:

$$\tilde{\rho}_1 := \frac{\bar{q}SdC_{Z_q}\cos\alpha}{2mV^2}; \quad \tilde{\rho}_2 := \frac{\bar{q}SC_{Z_{\delta_1}}\cos\alpha}{mV}; \quad \tilde{\rho}_3 := \frac{\partial q_{\mathrm{eq}}}{\partial\alpha};$$
$$\tilde{\rho}_4 := \frac{\partial\delta_{q,\mathrm{eq}}}{\partial\alpha}; \qquad \tilde{\rho}_5 := \frac{\bar{q}Sd^2C_{m_q}}{2I_{\mathrm{yy}}V}; \qquad \tilde{\rho}_6 := \frac{\bar{q}SdC_{m_{\delta_1}}}{I_{\mathrm{yy}}} \tag{11}$$

As a consequence, the state matrix can be expressed as a function of the new set $\tilde{\rho}(t)$ as in Eq. (12). The reformulated state matrix $A(\tilde{\rho})$ is still nonaffine in the original set of scheduling variables $\rho(t)$, but it is affine in the new set $\tilde{\rho}(t)$ as desired. However, this formulation relies on a large set of scheduling functions, $n_{\tilde{\rho}} = 6$, unfeasible for controller design purposes:

$$A(\tilde{\rho}) = \begin{bmatrix} 0 & (1+\tilde{\rho}_1) & \tilde{\rho}_2 \\ 0 & \tilde{\rho}_5 - \tilde{\rho}_3(1+\tilde{\rho}_1) & \tilde{\rho}_6 - \tilde{\rho}_3\tilde{\rho}_2 \\ 0 & -\tilde{\rho}_4(1+\tilde{\rho}_1) & -\tilde{\rho}_4\tilde{\rho}_2 \end{bmatrix} \tag{12}$$

It is important to notice that a different parameterization of the state matrix would result in a different set of scheduling functions. This step requires extensive knowledge of the system dynamics under investigation.

b. Analysis. To reduce the number of identified scheduling functions, their variation is analyzed as a function of the original set of parameters $\rho(t)$. Indeed, $\rho(t)$ represents the envelope of all the flight conditions characterizing the projectile's trajectory as a convex subspace (polytope). Any trial scheduling function in $\tilde{\rho}(t)$, which is highly varying inside the original polytope, must be maintained, while the functions with limited effect on the system dynamics might be approximated or completely neglected. The evaluation is based on the flight envelope defined by $\alpha \in [0, 16]$ deg, $V \in [160, 280]$ m/s, and $h \in [1, 14]$ km. Because the design aims at improving the range capability of the projectile, only positive values of AoA are considered. Similarly, $h = 14$ km corresponds to the maximum apogee conditions estimated for the range optimization, while $h = 1$ km is assumed as the altitude level where the transition from the gliding phase to the terminal guidance occurs.

First, the scheduling function $\tilde{\rho}_1$ is investigated. The results in Fig. 2 show the variation of $\tilde{\rho}_1$ as a function of the airspeed and the altitude in the selected ranges. In particular, the variation of $\tilde{\rho}_1$ is computed at increasing values of altitude, with an increment of $\Delta h = 1$ km (blue lines). Because of the low order of magnitude, the variation of $\tilde{\rho}_1$ has a negligible impact on the system dynamics at

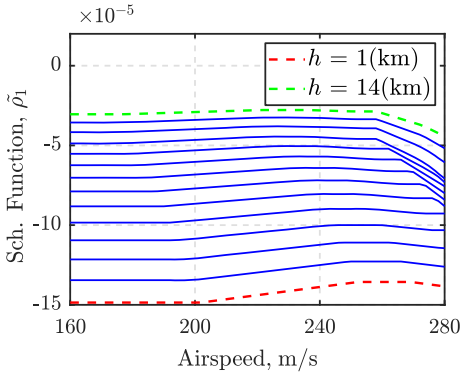

Fig. 2 Approximation analysis: $\tilde{\rho}_1$ at $\alpha = 12$ deg.

any (V, h) flight conditions. The results concerning the variation of $\tilde{\rho}_1$ as a function of the AoA provide the same conclusion and are not shown for brevity. As a consequence, the following approximation holds:

$$\tilde{\rho}_1 \approx 0 \mid A_{12}(\tilde{\rho}) = (1 + \tilde{\rho}_1) \approx 1$$

As observed in Eq. (11), the functions $\tilde{\rho}_2$, $\tilde{\rho}_5$, and $\tilde{\rho}_6$ have a common affine dependence on the dynamic pressure value $\bar{q}$. In particular, the definition of $\bar{q}$ itself includes the variations of two original scheduling variables: V and h. Thus, the three scheduling functions can be approximated uniquely as linear functions of the dynamic pressure. All the remaining parameters affecting $\tilde{\rho}_2$, $\tilde{\rho}_5$, and $\tilde{\rho}_6$ are frozen to a nominal average value $(\bar{V}, \bar{C}_{Z_{\delta_1}}, \bar{C}_{m_q}, \bar{C}_{m_{\delta_1}})$ in their range of variations, leading to the approximations:

$$\bar{\rho}_2(\bar{q}) = \frac{\bar{q}S\bar{C}_{Z_{\delta_1}}}{m\bar{V}} \approx \tilde{\rho}_2; \qquad \bar{\rho}_5(\bar{q}) = \frac{\bar{q}Sd^2\bar{C}_{m_q}}{2I_{yy}\bar{V}} \approx \tilde{\rho}_5;$$
$$\bar{\rho}_6(\bar{q}) = \frac{\bar{q}Sd\bar{C}_{m_{\delta_1}}}{I_{yy}} \approx \tilde{\rho}_6 \tag{13}$$

In particular, the aerodynamic coefficients are functions of the Mach value, hence of V and h, but their variations are very limited, thus negligible. Similarly, the impact of the AoA variation on $\tilde{\rho}_2$ is assumed negligible for the present analysis. The accuracy of these approximations is verified at each flight condition (V, h) as the root mean square error evaluated in the full range of $\alpha = [0, \ldots, 16] \in \mathbb{R}^N$ and normalized (NRMSE) by the mean value of the original scheduling function at the same flight point:

$$\text{NRMSE}_{\tilde{\rho}_j}(V, h) := \frac{\sqrt{\frac{\sum_{i=1}^{N}(\tilde{\rho}_j(\alpha_i,V,h) - \bar{\rho}_j(\alpha_i,V,h))^2}{N}}}{\frac{\sum_{i=1}^{N}\tilde{\rho}_j(\alpha_i,V,h)}{N}}; \qquad j \in [2, 5, 6]$$

The results related to $\tilde{\rho}_2$ are shown in Fig. 3a. The approximation error is minimum at the airspeed conditions around the selected nominal value, $\bar{V} = 220$ m/s. However, it does not exceed 20% in the main range of variation occurring during the gliding phase, regardless of the (α, h) values. Similarly, the accuracy of $\tilde{\rho}_5$ is lower at lower airspeed values (less than or equal to 20%) and improves at higher conditions (less than or equal to 10%). Indeed, conditions of $V \geq 240$ m/s never occur at low altitude levels, due to the characteristic gliding trajectory of the projectile. Thus, the upper curves on the right half of Fig. 3b are not relevant to the analysis. Finally, the approximation of $\tilde{\rho}_6$ provides extremely accurate results as observed in Fig. 3c. Indeed, this function is not dependent on the inverse of V, as the previous, but only on the dynamic pressure. All the previous results are summarized in Table 1.

Table 1 Normalized root mean square errors

Functions	NRMSE maximum	NRMSE minimum	Reference error, %
$\tilde{\rho}_2$	0.31	0.02	20
$\tilde{\rho}_5$	0.25	0.001	10
$\tilde{\rho}_6$	0.064	0	2

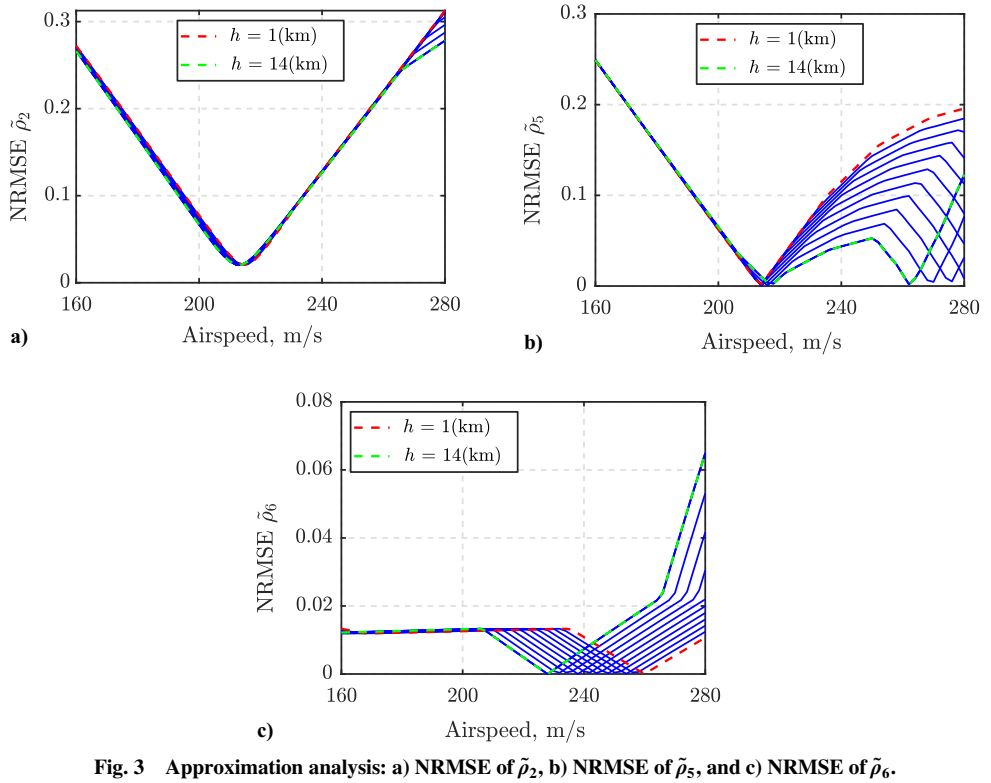

Fig. 3 Approximation analysis: a) NRMSE of $\tilde{\rho}_2$, b) NRMSE of $\tilde{\rho}_5$, and c) NRMSE of $\tilde{\rho}_6$.

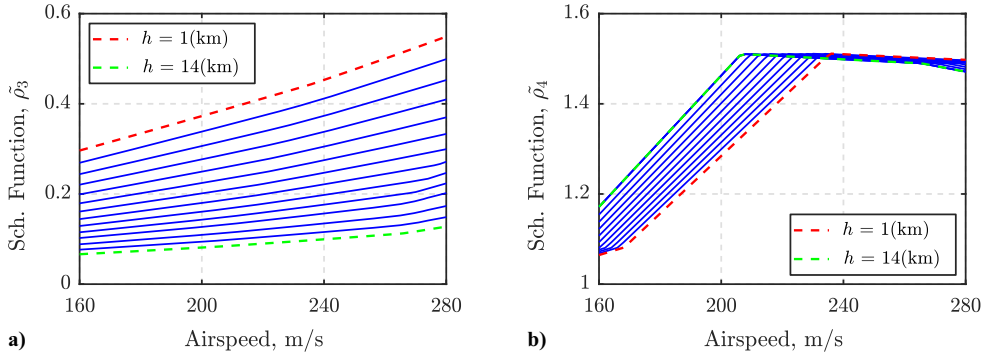

Fig. 4 Approximation analysis: a) $\tilde{\rho}_3$ variation at $\alpha = 12$ deg and b) $\tilde{\rho}_4$ variation at $\alpha = 12$ deg.

Based on the analysis, the approximations in Eq. (13) hold, and the variation of three scheduling functions ($\tilde{\rho}_2$, $\tilde{\rho}_5$, and $\tilde{\rho}_6$) can be represented in terms of the dynamic pressure variation only. By including $\bar{q}$ instead of $\tilde{\rho}_2$, $\tilde{\rho}_5$, and $\tilde{\rho}_6$ in the new scheduling vector, the corresponding dimension $n_{\tilde{\rho}}$ reduces significantly.

Concerning the remaining functions $\tilde{\rho}_3$ and $\tilde{\rho}_4$ the curves in Figs. 4a and 4b, respectively, reveal the highly nonlinear behavior characterizing the derivatives of the equilibrium functions $\partial q_{\text{eq}}/\partial\alpha$ and $\partial\delta_{q,\text{eq}}/\partial\alpha$. Additionally, their complex symbolic expressions prevent any possible parameterization as a linear function of the dynamic pressure or of the original set of scheduling variables. As a consequence, they are directly assumed as new scheduling functions, leading to the definition of the final scheduling vector, $\hat{\rho} = [\hat{\rho}_1, \hat{\rho}_2, \hat{\rho}_3]$, as:

$$\hat{\rho}_1 := \bar{q}; \qquad \hat{\rho}_2 := \frac{\partial q_{\text{eq}}}{\partial\alpha}; \qquad \hat{\rho}_3 := \frac{\partial\delta_{q,\text{eq}}}{\partial\alpha} \tag{14}$$

Consistently, the state matrix in Eq. (12) can be reformulated in a parameter affine form as:

$$\tilde{A}(\hat{\rho}) = \begin{bmatrix} 0 & 1 & \bar{A}_{13}(\hat{\rho}_1) \\ 0 & \bar{A}_{22}(\hat{\rho}_1) - \hat{\rho}_2 & \bar{A}_{23}(\hat{\rho}_1) \\ 0 & -\hat{\rho}_3 & -\hat{\rho}_3\bar{A}_{13}(\hat{\rho}_1) \end{bmatrix} \tag{15}$$

where $\bar{A}_{13} = \bar{\rho}_2$ and $\bar{A}_{22} = \bar{\rho}_5$ are the approximated forms of $\tilde{\rho}_2$ and $\tilde{\rho}_5$, respectively, discussed in Eq. (13). As a final approximation, the matrix entry $\bar{A}_{23} = \frac{\bar{q}Sd\bar{C}_{m_{\delta_1}}}{I_{yy}} - \hat{\rho}_2\bar{A}_{13} \approx \frac{\bar{q}Sd\bar{C}_{m_{\delta_1}}}{I_{yy}}$ since the term $\hat{\rho}_2\bar{A}_{13}$ is negligible.

c. Verification. To assess the accuracy of the overall procedure, Figs. 5a and 5b show a comparison between the pole-zero maps of the original (full) and the approximated (aprx.) models. Specifically, Fig. 5a corresponds to stable flight conditions, assuming $\alpha = 12$ deg and increasing values of V and h, while Fig. 5b compares a stable ($\alpha = 10$ deg) and an unstable ($\alpha = 7$ deg) configuration for increasing values of V and a constant $h = 8$ km. Different axes scales are selected to improve the readability of the presented results. A slight difference between the original and the approximated poles is observed, especially for higher values of V and lower values of h. However, the effects of the approximations do not generate relevant modifications in the system dynamics, confirming the accuracy of the modeling procedure. These new sources of uncertainties are addressed at the control design stage, discussed in the next section.

2. *Polytope's Dimensions Reduction*

The second step of the procedure focuses on the analysis of the convex polytope defined by the new set of scheduling functions, $\hat{\rho} = [\hat{\rho}_1(V,h), \hat{\rho}_2(\alpha,V,h), \hat{\rho}_3(\alpha,V,h)]$. Indeed, it is necessary to properly map the original envelope, $\alpha \in [0, 16]$ deg, $V \in [160, 280]$ m/s, and $h \in [1, 14]$ km, into the corresponding new one, $\hat{\rho}_j \in [\underline{\hat{\rho}_j}, \overline{\hat{\rho}_j}]$, with $j = 1, 2, 3$, and where $\overline{\hat{\rho}_j}$ and $\underline{\hat{\rho}_j}$ are scheduling functions the upper and lower bounds, respectively, to define the vertices of the new polytope. The following steps allow for estimating the upper and lower values of each scheduling function $\hat{\rho}_j$ across the entire set of flight conditions described by α, V, and h.

a. Selection. Because the scheduling functions in $\hat{\rho}$ are highly nonlinear, the flight envelope is sampled into a fine 3D grid of flight points (α, V, h). However, the scheduling functions are evaluated only on a subset of the overall grid, which respects the physical constraints affecting the variables. Indeed, Fig. 6 shows the specific relationship characterizing h/V in a standard gliding phase trajectory scenario. The trajectory was obtained through a closed-loop guidance simulation, employing a simplified planar point-mass model of the projectile dynamics. The figure shows how certain (h, V) conditions are inconsistent with the targeted projectile's trajectory; thus, they must be neglected in the mapping process. As a first form of polytope reduction, a cluster of n_c flight conditions (red points) is selected only around the reference trajectory. The selection of the n_c points relies on a process where a progressively finer grid of conditions has been employed for a more accurate estimation of the boundaries of each scheduling function. The final 3D design grid additionally accounts for the range of variation of the AoA, as shown in Fig. 7a.

b. Map. The scheduling functions in $\hat{\rho}$ are evaluated across the selected n_c flight points, generating a new 3D convex subspace,

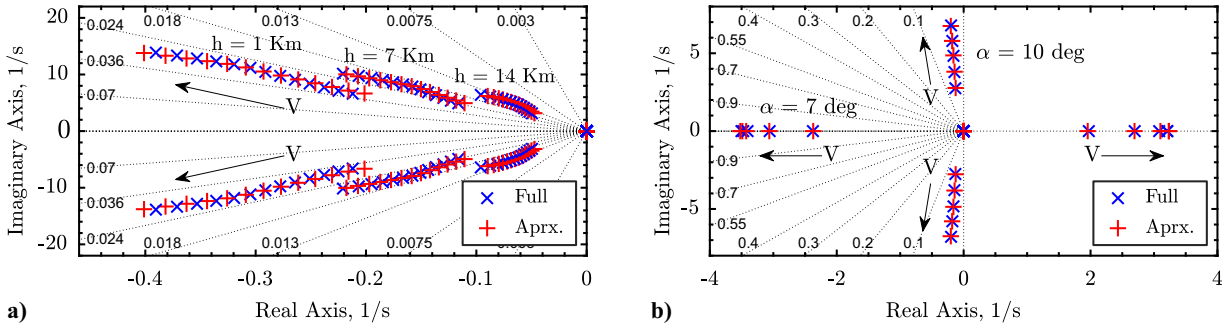

Fig. 5 Pole-zero maps: a) (V, h) variation at $\alpha = 12$ deg and b) stable/unstable α conditions.

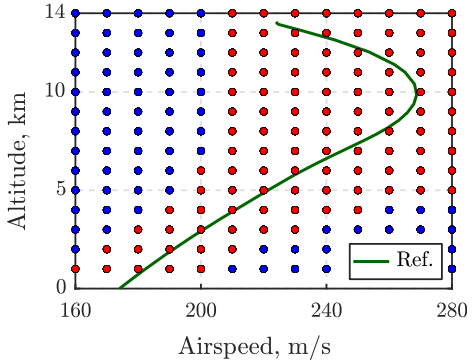

Fig. 6 Flight points selection: $V - h$ trajectory constraints.

as in Fig. 7b. The vertices of the new polytope are defined by the boundary values for each scheduling function: $\hat{\rho}_1 \in [0.5, 3] \times 10^4$, $\hat{\rho}_2 \in [0.05, 0.5]$, and $\hat{\rho}_3 \in [-1, 4]$. The new polytope is still affected by a certain level of conservatism because the selection of the grid points was based on an approximated reference trajectory.

c. Reduction. By employing the polytope defined in step 2b, it is possible to design a first LPV polytopic controller, as detailed in the following section, and test the closed-loop system in the nonlinear simulator environment. During the tests, the online evaluation of the scheduling functions $\hat{\rho}$ allows for redefining the boundaries of the polytope, based on more accurate and realistic trajectories. Indeed, the initial selection of flight conditions in Fig. 6 is affected by a certain level of conservatism. By iteratively adjusting the dimensions of the polytope and updating the controller design, it is possible to significantly reduce the ranges of the scheduling functions to $\hat{\rho}_1 \in [0.5, 2] \times 10^4$, $\hat{\rho}_2 \in [0.05, 0.35]$, and $\hat{\rho}_3 \in [-1, 2]$, as shown in Fig. 7c. Because inconsistent flight conditions are neglected, the controller design results are progressively less affected by optimization conservatism.

IV. Polytopic Controller Design

In this section, the controller design methods and objectives are presented. The overall generalized plant architecture is first introduced, followed by the formulation of the LPV $\mathcal{H}_\infty$ controller optimization problem. The controller synthesis addresses the flight envelope represented by the variation of the scheduling variables: $\alpha \in [0, 16]$ deg, $V \in [160, 280]$ m/s, and $h \in [1, 14]$ km. The polytope is defined through the corresponding ranges of variation of the new set of scheduling functions $(\hat{\rho}_1, \hat{\rho}_2, \hat{\rho}_3)$ obtained in Sec. III as a result of the approximation process.

The LPV $\mathcal{H}_\infty$ polytopic approach allows directly shaping the frequency properties of the closed-loop system, guaranteeing stability and performance at any flight conditions belonging to the polytope. Indeed, if the frequency constraints are respected at each vertex of the polytope, the same performances are guaranteed for any controller interpolated at intermediate flight conditions.

A. Generalized Plant Architecture

The general architecture employed for the controller design is presented in Fig. 8a. A second-order model is included in the definition of the generalized plant to account for the actuator dynamics, together with the approximated polytopic quasi-LPV model described in Eqs. (14) and (15). A set of first-order weighting functions W_e and W_u imposes the desired closed-loop performances by targeting the tracking error, $e = r - \alpha$, and the derivative of the control deflection input $\dot{\delta}_{q,\text{cmd}}$, respectively. The reference signal r consists of an AoA trajectory defined through a *lift-to-drag* ratio optimization law [38,39]. The weighting functions are selected to achieve a suitable compromise between tracking capability, disturbance rejection, and overall order of complexity.

Because tracking capability and disturbance rejection are conflicting properties, they cannot be simultaneously optimized through the imposition of a single filter. The bandwidth of W_e is dedicated to ensuring a reliable output disturbance rejection to the system, while a first-order reference model f_{ref} sets the desired time response the system should achieve. An additional first-order weighting function W_r is applied to the resulting response error, $e_r = f_{\text{ref}} - \alpha$, to impose tighter bandwidth restrictions and improve the tracking capability of the guidance reference signal. In particular, a core objective of the reference model selection relies on minimizing the overshoot affecting the system response. Indeed, in a gliding flight scenario, the guidance reference signal is generally engaged at the apogee of the projectile's trajectory, generating sudden and sharp variation in the projectile's attitude. A large overshoot on the AoA might lead to the saturation of the aerodynamic control surfaces, critical for control purposes.

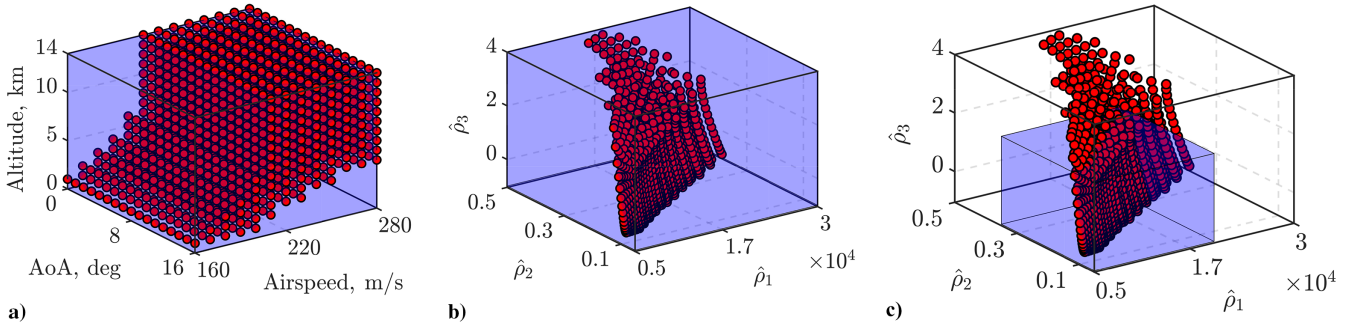

Fig. 7 Polytope maps: a) (α, V, h) subspace, b) $(\hat{\rho}_1, \hat{\rho}_2, \hat{\rho}_3)$ subspace, and c) reduced $(\hat{\rho}_1, \hat{\rho}_2, \hat{\rho}_3)$ subspace.

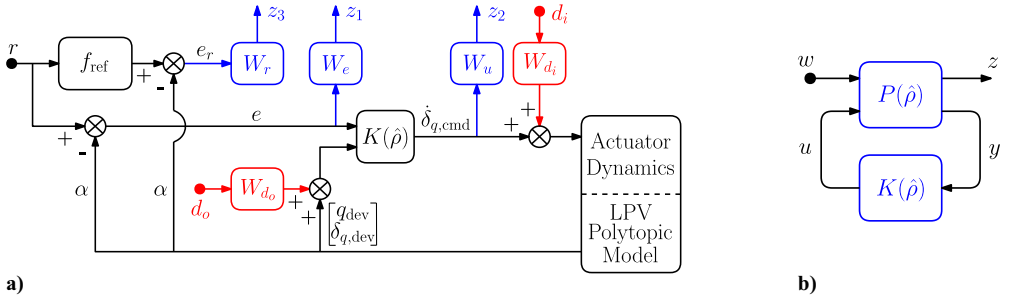

Fig. 8 Design scheme: a) detailed architecture and b) general control configuration.

Concerning the control input, the rolloff frequency of W_u is selected in accordance with the characteristic bandwidth of the actuator model to prevent stall events. Additionally, constant weights, $W_{d_i} = 0.1$ and $W_{d_o} = 0.1$, are applied to the input and output disturbance signals d_i and d_o, respectively, aiming to properly scale the disturbance effects on the model. As a relevant remark, the weighting functions are independent of the scheduling functions, meaning that the same performances are imposed at each vertex condition of the polytope, leading to possible conservativeness in the synthesis results.

The control scheme in Fig. 8a is then generalized as in Fig. 8b, where the LPV plant $P(\hat{\rho})$ includes the dynamics of the actuator, the projectile polytopic model, the reference model, and the weighting functions. Thus, the overall generalized state vector is defined as $x_P = [x,\ x_{\text{act}},\ x_{\text{ref}},\ x_{W_e},\ x_{W_u},\ x_{W_r}]^T \in \mathbb{R}^9$, with $x = [\alpha,\ q_{\text{dev}},\ \delta_{q,\text{dev}}]^T \in \mathbb{R}^3$. The generalized exogenous input vector, $\omega = [r,\ d_i,\ d_o]^T \in \mathbb{R}^3$, accounts for the reference guidance signal and the input and output disturbances, while the generated control input, $u \in \mathbb{R}$, corresponds to the commanded virtual pitch deflection rate $\dot{\delta}_{q,\text{cmd}}$ imposed on the canards. Indeed, the result of the inclusion of the integrator dynamics during the state transformation process is the redefinition of the quasi-LPV model input σ as the derivative of δ_q. Finally, the generalized controlled output vector, $z = [z_1,\ z_2,\ z_3]^T \in \mathbb{R}^3$, includes the control optimization objectives, while the set of available measurements, $y = [e,\ q_{\text{dev}},\ \delta_{q,\text{dev}}]^T \in \mathbb{R}^3$, is employed as input to the controller. In the LPV polytopic control design, the generalized plant is evaluated at each flight condition corresponding to a vertex of the polytope, by substituting the corresponding values of the scheduling functions. The resulting LTI system realizations are employed in the formulation of the set of linear matrix inequalities (LMIs) that defines the controller synthesis optimization.

B. $\mathcal{H}_\infty$ Controller Synthesis

In the standard $\mathcal{H}_\infty$ robust control framework, the design aims to minimize the closed-loop induced L_2 norm, of the defined generalized plant, such that:

$$\|z\|_2 \leq \gamma_\infty \|w\|_2; \qquad \gamma_\infty > 0 \tag{16}$$

The index γ_∞ in Eq. (16) expresses how closely the frequency properties of the obtained closed-loop system match the desired performances, imposed through the weighting functions.

In the specific case of the LPV polytopic design, the controller synthesis is formulated as the resolution of a convex optimization problem, defined by the imposition of the same closed-loop performances at each realization of the LPV system. Thus, the optimization problem consists of a set of LMIs computed at each vertex of the polytope and solved offline through the identification of a constant Lyapunov function that guarantees the same stability and performance for each flight condition belonging to the polytope [24]. The solution corresponds to a set of LTI local controllers K_i, one for each of the Vx_i vertices, with $i = 1, \cdots, 8$. The general polytopic controller $K(\hat{\rho})$ for any combinations of the scheduling functions vector is obtained through the convex interpolation of the set of LTI controllers:

$$K(\hat{\rho}) = \sum_{i=1}^{8} \mu_i(\hat{\rho}) K_i$$

The design results obtained with the LPV $\mathcal{H}_\infty$ technique are investigated in the frequency domain in Fig. 9. Each figure represents a specific closed-loop property of the system, evaluated at each of the eight vertex conditions of the polytope (blue lines). As a first observation, Fig. 9a shows how the peak of the output Sensitivity function remains less than or equal to 6 dB for each curve, ensuring reliable stability margins at the vertices of the polytope. The transient dynamics of the system tend to be slightly less responsive due to the LMIs optimization which satisfies simultaneously the frequency requirements at each of the flight conditions. Therefore, the polytopic design is generally affected by a certain level of conservativeness, possibly deteriorating the performance of the controller. However, the employment of the pair of weighting functions (W_e, W_r) successfully imposes a reasonable bandwidth to the output Sensitivity and considerably improves the low-frequency disturbance rejection capability of the system, as shown in Fig. 9c. The latter property is fundamental to guaranteeing the controller can handle not only the uncertainties introduced during the modeling and approximation procedure but especially the external disturbances affecting the operating conditions of the projectile (e.g., wind contributions).

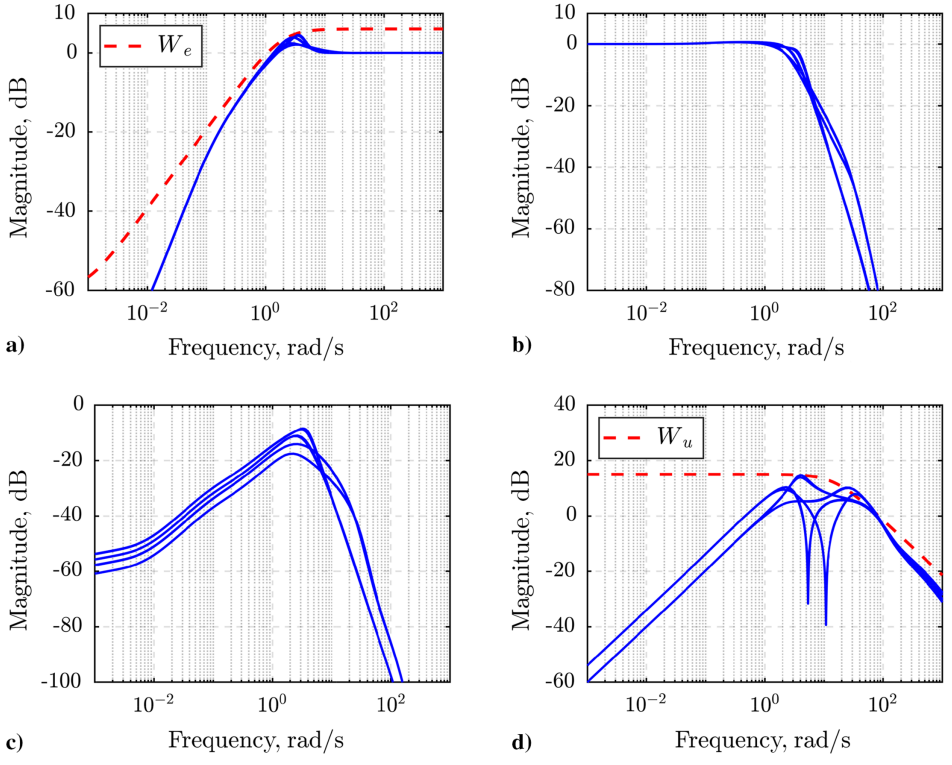

Fig. 9 Frequency results: a) sensitivity function, b) complementary sensitivity, c) plant sensitivity, and d) controller sensitivity.

Similarly, the polytopic design provides reliable high-frequency noise attenuation to handle possible distortion affecting the measurements, as shown in Fig. 9b. Indeed, the peaks of the Complementary Sensitivity functions are maintained at less than or equal to 1 dB. Concerning the performances imposed on the control effort by the weighting function W_u, the controller respects the limitations at all the flight conditions, both in terms of the operating bandwidth and in terms of the low-frequency steady-state amplitude, as shown in Fig. 9d. The presence of the reference model increases the effort required by the actuators to provide the desired performance, but the limitations guarantee considerable margins from saturation occurrences.

V. Trajectory Tracking Simulation

In this section, the LPV polytopic controller is tested in a trajectory tracking simulation scenario. The controller is implemented in a complete nonlinear simulator environment to verify its capability to handle all the possible uncertainties introduced by the modeling and approximation process.

The reference signal corresponds to a realistic AoA trajectory α_{ref} generated through the online evaluation of a range-extending guidance law, based on the lift-to-drag ratio optimization. The simulation aims to cover most of the range of variation of each scheduling function to assess the performances of the controller and to verify which areas of the polytope are interested in the trajectory.

A. Simulator Architecture

The scheme in Fig. 10 presents the overall nonlinear simulator environment, developed in a previous work [36]. Besides the implementation of the polytopic controller and the actuator dynamics, the nonlinear simulator also targets the following aspects.

1. Guidance

This block implements the online lift-to-drag ratio optimization law proposed in [39]. The algorithm provides a tradeoff between highly complicated head-on approaches and suboptimal architecture based on a set of open-loop offline evaluations of standard pitch-attitude dynamics. Assuming quasi-steady state glide equilibrium conditions with approximately constant dynamic pressure for two-DoF pitch-attitude dynamics and assuming that an optimal lift-to-drag ratio $\text{LD}_{\max}$ exists at each flight condition, the corresponding equilibrium flight-path angle γ_{eq} can be expressed as:

$$\gamma_{\text{eq}} = -\frac{1}{\text{LD}_{\max}\left|1 + \beta_{\text{atm}}\left(\frac{V^2}{2g}\right)\right|}$$

where $\beta_{\text{atm}} = 1.389 \cdot 10^{-4}$ 1/m represents the exponent of the atmosphere density, modeled as $\rho_{\text{atm}} = \rho_{\text{atm},0} e^{-\beta_{\text{atm}} h}$ with $\rho_{\text{atm},0} = 1.227\ \text{kg/m}^3$. A reference AoA command α_{ref} can be derived from the combination:

$$\alpha_{\text{ref}} = \alpha_{\text{LD,max}} + k_\gamma(\gamma_{\text{eq}} - \gamma)$$

where $\alpha_{\text{LD,max}}$ consists of the optimal AoA, obtained by trimming the pitch-attitude dynamics at each $\text{LD}_{\max}$ condition and γ is the actual flight-path angle measured along the trajectory. The coefficient k_γ allows adjusting the relevance of the flight-path angle correction with respect to the trimmed $\alpha_{\text{LD,max}}$, aiming to find an optimal tradeoff and to avoid excessively sharp variation of the resulting reference signal. For the present study, $k_\gamma = 0.35$ has been selected, and a data set of $(\text{LD}_{\max}, \alpha_{\text{LD,max}})$ has been provided through dedicated CFD campaigns on the complete projectile dynamics to increase the accuracy.

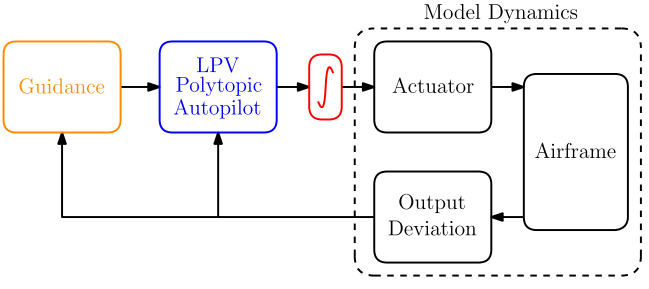

Fig. 10 Nonlinear simulator environment.

2. Actuator

The actuators are modeled as second-order systems characterized by the transfer function:

$$T_\delta = \frac{\omega_\delta}{s^2 + 2\omega_\delta \xi_\delta s + \omega_\delta^2}$$

where $\omega_\delta = 150$ rad/s is the actuator bandwidth and $\xi_\delta = 0.707$ represents the damping ratio. Additionally, the saturation affecting the angular position and angular rate is also addressed.

3. Airframe

The airframe block contains a complete description of the flight mechanics, the environment, and the generation of the aerodynamic contributions, as presented in Fig. 11. In particular, the environment model provides a general model for the atmosphere following the International Standard Atmosphere (ISA) 1975, ISO 2533 [40]. In addition, it targets the wind contributions (shear, gusts, and turbulence), employed as sources of disturbance to assess the robustness of the controller in more realistic scenarios. Concerning the *Aerodynamic Model*, the general *Multivariable* static model and the complete control contributions described in Appendix B are employed in the simulator environment. Based on a significant CFD data set, this model allows accounting for all the possible flight configurations the projectile might experience during the trajectory. Indeed, the simultaneous variations of $\mathcal{M}$, α, and β are considered in the formulation of the aerodynamic forces and moments. The flight mechanics block implements the six-DoF model of the projectile, including the kinematic and dynamic equations of motion provided in Appendix A. Finally, the control allocator converts the individual right and left canards' deflections into a combined pitch and roll contribution, as previously expressed in Eq. (3).

4. Output Deviation

The output of the six-DoF nonlinear model is partially adjusted in postprocessing in order to comply with the formulation of the quasi-LPV pitch channel dynamics employed for the controller design. Indeed, the output of the model in Eqs. (7) and (8), obtained through the State Transformation approach, consists of the off-equilibrium states q_{dev} and $\delta_{q,\text{dev}}$. Because these measurements are employed as input to the LPV controller, the output of the overall six-DoF nonlinear model needs to be *deviated* consistently by evaluating online the equilibrium functions q_{eq} and $\delta_{q,\text{eq}}$ at each flight condition. These implementation solutions can result in additional sources of model uncertainties that may affect the robustness properties of the controller.

As a final remark, the quasi-LPV model was augmented with an integrator at the plant's input to cancel the internal feedback loop affecting the stability of the system. Thus, an integrator is interposed between the output of the controller and the input of the actuator model in the nonlinear simulator of Fig. 10 to ensure consistency.

B. Simulation Results

The complete ballistic-gliding trajectory results of the projectile simulation are shown in Fig. 12. The trajectory is expressed in the

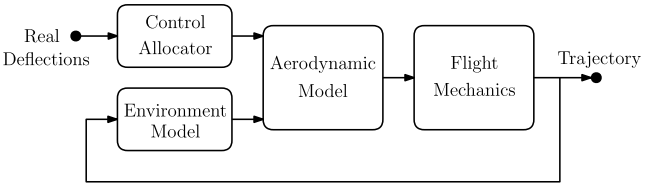

Fig. 11 Airframe simulation scheme.

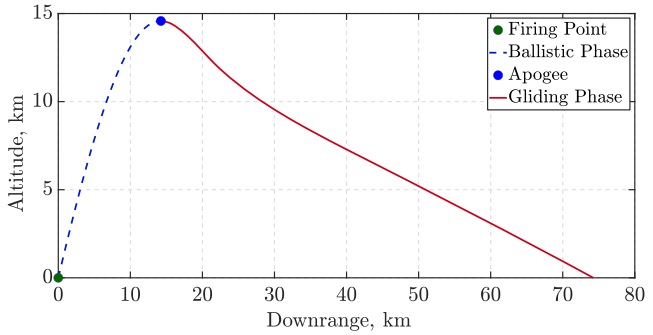

Fig. 12 Simulation results: projectile's full trajectory.

local-level coordinates. An initial firing angle, $\theta_0 = 60$ deg, and an initial velocity, $V_0 = 939$ m/s, are set to reach the desired apogee conditions. During the ballistic phase, the canards are folded in the sabot of the projectile to minimize the aerodynamic drag and avoid any destabilizing lift contribution. Once the apogee is reached, the canards are deployed and set with an initial zero local pitch deflection δ_{q_0}, and the guidance evaluation algorithm is launched.

A sudden rise in the AoA is observed in Fig. 13a, corresponding to the initialization of the controller and the tracking of the guidance reference. As desired, the overshoot generated by the initialization is handled by the controller, which rapidly stabilizes and converges to the reference signal, minimizing the tracking error (less than or equal to 1% at the steady state) for the rest of the trajectory. Additionally, Fig. 13b shows how the total pitch deflection of the canards α_{can} is maintained at a relatively low amplitude during the entire trajectory, far below the saturation limits. The total pitch deflection corresponds to the overall deflection angle perceived by the canards, expressed as the linear superposition between the local pitch deflection commanded by the controller and the AoA characterizing the trajectory of the projectile, as $\alpha_{\text{can}} = \alpha + \delta_{q,\text{cmd}}$.

The results in Fig. 14a allow for verifying the relation $V - h$. Despite the different apogee conditions, the simulation results belong perfectly to the areas of the flight envelope considered during the polytopic modeling process. The reference trajectory (dashed green) represents the guidance point-mass model simulations previously presented in Fig. 6 and employed in the selection of the grid points. Coherently, Fig. 14b shows that the entire gliding phase of the trajectory occurs at a subsonic-transonic regime, with $\mathcal{M} < 1$ as expected.

Concerning the polytope dimensions, Figs. 15a–15c present the simulation trajectories related to the scheduling functions $\hat{\rho}_1, \hat{\rho}_2$, and $\hat{\rho}_3$, respectively. As a first observation, all the trajectories perfectly belong to the boundaries imposed through the definition of the polytope. The function $\hat{\rho}_3$ is characterized by an evident dependence on the variation of the AoA because the trajectories have very similar shapes. As a consequence, $\hat{\rho}_3$ is subjected to a sudden and sharp increment causing the variation rate $\dot{\hat{\rho}}_3 \to \infty$. This observation exploits one of the main advantages of LPV polytopic design compared to the standard gain-scheduling strategy. Indeed, one of the major limitations affecting gain-scheduling design relies on the lack of performance guarantees in the case of rapid variation of scheduling parameters. Differently, the polytopic approach allows accounting for an infinite variation rate, under the condition of an affine model-parameter relation.

As a further source of analysis, Fig. 15d exhibits the trajectories of the controller interpolation functions associated with each of the LTI local controllers designed at the vertices of the polytope. The data in Table 2 provide an overview of the relevance of each local controller (at the Vx_i vertex, with $i = 1, \cdots, 8$) on the overall interpolation process across the entire trajectory of the projectile. As expected, Vx_1 and Vx_3 show a prevalent percentage in the controller interpolation at the beginning of the simulation, while the influence of Vx_6 and Vx_8 increases along with the trajectory and provides on average the most relevant contributions. Despite the fact that the 3D trajectory of the scheduling functions in Fig. 16 seems to be quite independent of the local controllers of Vx_4, Vx_5, and Vx_7, the results in Table 2 show their nonnegligible role in the interpolation. On the contrary, the last controller Vx_2 appears to be generally of marginal importance.

The restricted subspace covered by the 3D trajectory in Fig. 16 suggests that a redefinition of the polytope's shape might further improve the optimization of the controller design.

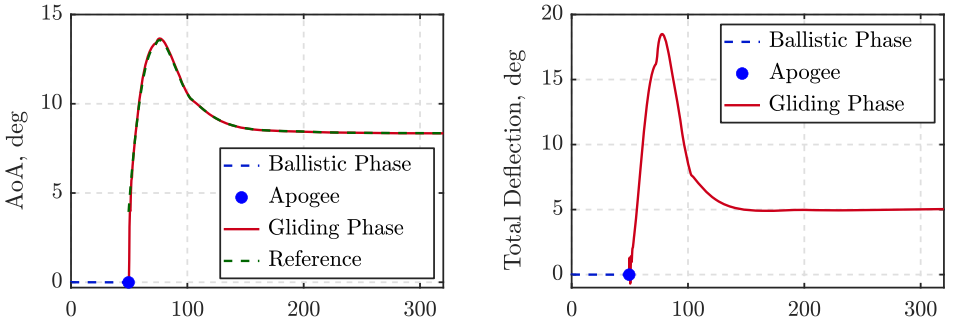

Fig. 13 Simulation results: a) AoA trajectories and b) total pitch deflection.

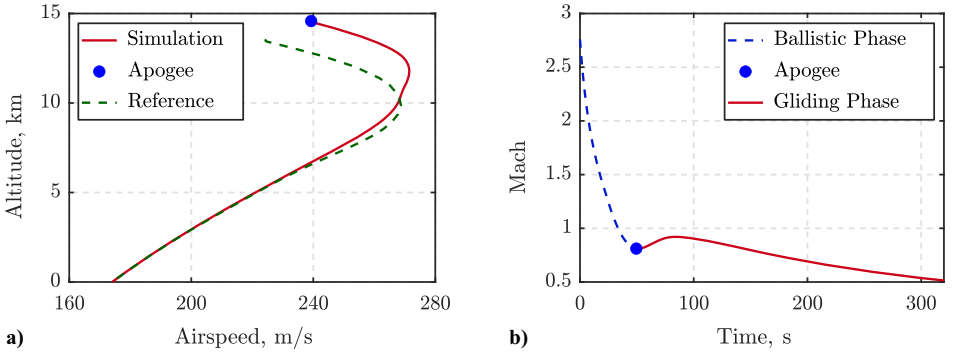

Fig. 14 Simulation results: a) $V - h$ physical relation and b) Mach number trajectory.

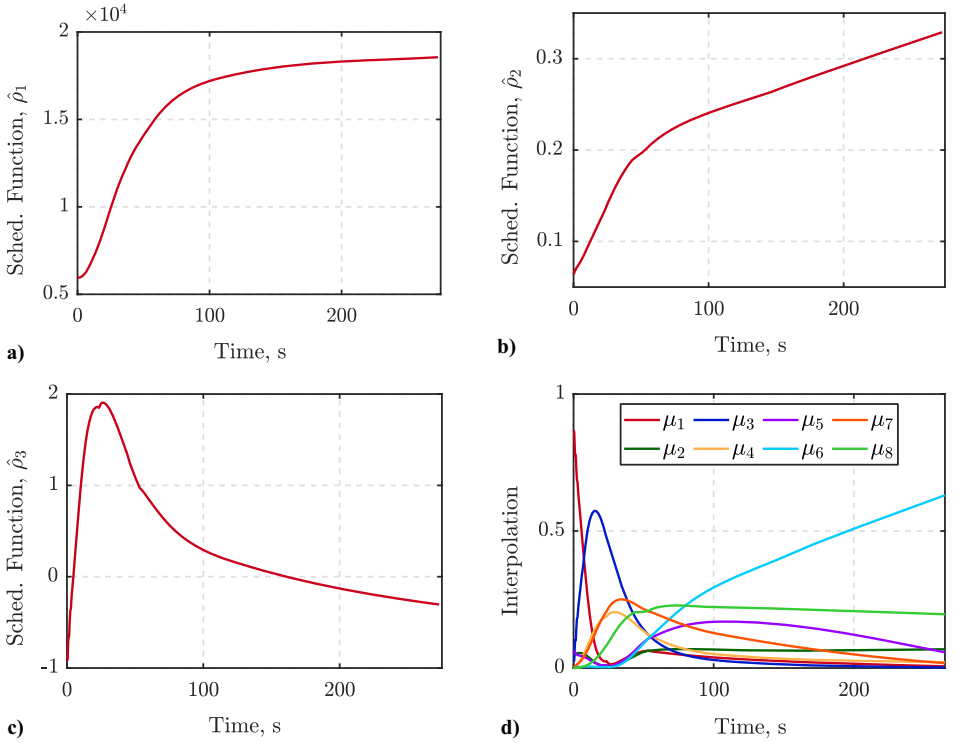

Fig. 15 Simulation results: a) scheduling function $\hat{\rho}_1$, b) scheduling function $\hat{\rho}_2$, c) scheduling function $\hat{\rho}_3$, and d) interpolation trajectories μ.

Table 2 Controller interpolation functions

Interpolation function	Vertices	$\hat{\rho}_1$	$\hat{\rho}_2$	$\hat{\rho}_3$	Maximum, %	Minimum, %	Average, %
μ_1	Vx_1	$0.5 \cdot 10^4$	0.05	−1	86	0.5	6
μ_2	Vx_2	$2 \cdot 10^4$	0.05	−1	7	0.6	5
μ_3	Vx_3	$0.5 \cdot 10^4$	0.05	2	57	0.1	10
μ_4	Vx_4	$2 \cdot 10^4$	0.05	2	20	0.1	6
μ_5	Vx_5	$0.5 \cdot 10^4$	0.35	−1	17	0.8	11
μ_6	Vx_6	$2 \cdot 10^4$	0.35	−1	65	0.3	32
μ_7	Vx_7	$0.5 \cdot 10^4$	0.35	2	26	0.2	10
μ_8	Vx_8	$2 \cdot 10^4$	0.35	2	25	≈0	19

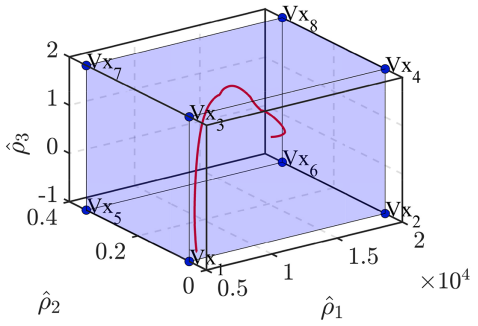

Fig. 16 Simulation results: scheduling functions in the 3D polytope.

The results of the simulation confirm the quality of the modeling and approximation process performed to convert the nonlinear pitch channel dynamics of the projectile into a quasi-LPV polytopic model as well as the advantages of the polytopic controller design. Indeed, the resolution of the set of LMIs only at the vertices of the polytope drastically reduces the overall computational complexity, allowing the synthesis of a controller able to stabilize the system at any flight conditions belonging to the polytope. As a drawback, the polytopic approach tends to generate conservative results that can deteriorate the performance of the controller. The employment of a systematic analysis of the scheduling variable ranges to optimize the polytope's dimensions reduces significantly the conservativeness of the controller synthesis, while leveraging guarantees provided by the LPV polytopic design.

VI. Conclusions

In this paper, a systematic procedure is proposed to model the nonlinear pitch channel dynamics of a new class of guided projectiles as a polytopic system. The nonlinear dynamics is first converted to a reliable quasi-LPV model, using the State Transformation method. The quasi-LPV model is later reformulated to comply with the polytopic requirements of an affine model-parameter relation through a process that maps the original set of scheduling variables into a new set of scheduling functions. The process requires an extensive investigation of the system dynamics to identify a suitable set of new scheduling functions, consistent with the original flight envelope. However, it allows modeling the flight envelope as a convex subspace (polytope) whose vertices correspond to the combination of the boundary values of each new scheduling function. Then, the LPV polytopic controller synthesis is performed, accounting for the design constraints imposed only at the vertices conditions of convex subspace, reducing the overall computational complexity. The synthesis results in a set of local realizations of the LPV controller corresponding to the each of polytope's vertices. Thus, the LPV controller, evaluated at any intermediate flight points belonging to the convex space, is obtained from the interpolation of a reduced set of local controllers, simplifying the implementation stage. As a main drawback, the polytopic approach tends to introduce conservativeness in the controller optimization synthesis. Thus, the final step of the proposed modeling procedure aims to adjust the ranges of variation of the new scheduling functions to optimize the dimensions of the polytope.

The controller design is based on the $\mathcal{H}_\infty$ mixed sensitivity approach. The frequency domain results show how the polytopic controller ensures relevant disturbance rejections, reliable tracking capability, and reasonable control effort requirements properties at all the investigated flight conditions. The controller is later implemented in a complete nonlinear simulator environment to assess its

performance in a gliding phase simulation scenario. A lift-to-drag ratio optimization guidance law is employed to generate a reference angle-of-attack trajectory that maximizes the operating range of the projectile. The results confirm the capability of the LPV polytopic controller to successfully stabilize the projectile dynamics across the entire flight envelope described by the polytope and to properly track the reference guidance signal. However, the trajectories of the controller interpolation functions reveal the limited relevance of the controller local realizations at certain vertices of the polytope. A redefinition of the polytope's shape might improve the LPV $\mathcal{H}_\infty$ design by neglecting those specific flight points in the overall optimization process.

Appendix A: Six-DoF Nonlinear Dynamics

The nonlinear dynamics of the guided projectile complies with the flight mechanics tensor formulation presented in [41]. The translational dynamics expresses the linear motion of the projectile's center of gravity, while the attitude dynamics represents the angular motion of the projectile's body frame B with respect to the inertial Earth frame E. These equations are projected into the system of coordinates associated with the projectile's body as in Eqs. (A1) and (A2), respectively:

$$\begin{bmatrix} \dot{u} \\ \dot{v} \\ \dot{w} \end{bmatrix} = \frac{1}{m}\begin{bmatrix} X \\ Y \\ Z \end{bmatrix} - \begin{bmatrix} 0 & -r & q \\ r & 0 & -p \\ -q & p & 0 \end{bmatrix}\begin{bmatrix} u \\ v \\ w \end{bmatrix} \tag{A1}$$

$$\begin{bmatrix} \dot{p} \\ \dot{q} \\ \dot{r} \end{bmatrix} = \begin{bmatrix} \frac{1}{I_{xx}} & 0 & 0 \\ 0 & \frac{1}{I_{yy}} & 0 \\ 0 & 0 & \frac{1}{I_{zz}} \end{bmatrix}\left(\begin{bmatrix} L \\ M \\ N \end{bmatrix} - \begin{bmatrix} 0 & -r & q \\ r & 0 & -p \\ -q & p & 0 \end{bmatrix} \times \begin{bmatrix} I_{xx} & 0 & 0 \\ 0 & I_{yy} & 0 \\ 0 & 0 & I_{zz} \end{bmatrix}\begin{bmatrix} p \\ q \\ r \end{bmatrix}\right) \tag{A2}$$

The projectile linear velocities are expressed by the state variables (u, v, w), whereas the angular velocities correspond to the triple (p, q, r). The external aerodynamic forces (X, Y, Z) and moments (L, M, N) are discussed in detail in the next section. Finally, I_{xx}, I_{yy}, and I_{zz} are the principal moments of inertia of the projectile's body, while m corresponds to the projectile's mass.

Appendix B: Aerodynamic Model

The aerodynamic forces and moments models in Eqs. (B1) and (B2), respectively, account for the static coefficient contributions $(C_{X_S}, C_{Y_S}, C_{Z_S}, C_{m_S}, C_{n_S})$, the damping coefficient contributions $(C_{Y_r}, C_{Z_q}, C_{l_p}, C_{m_q}, C_{n_r})$, the control coefficient contributions $(C_{X_{\delta_{\text{eff}}}}, C_{Z_{\delta_q}}, C_{l_{\delta_p}}, C_{m_{\delta_q}})$, and the gravitational contributions g based on the parameterizations:

$$\begin{bmatrix} X \\ Y \\ Z \end{bmatrix} = \bar{q}S\left\{\begin{bmatrix} C_{X_S}(\mathcal{M},\alpha,\beta) \\ C_{Y_S}(\mathcal{M},\alpha,\beta) \\ C_{Z_S}(\mathcal{M},\alpha,\beta) \end{bmatrix} + \left(\frac{d}{2V}\right)\begin{bmatrix} 0 \\ C_{Y_r}(\mathcal{M})r \\ C_{Z_q}(\mathcal{M})q \end{bmatrix} + \begin{bmatrix} C_{X_{\delta_{\text{eff}}}}(\mathcal{M},\delta_{\text{eff}}) \\ 0 \\ C_{Z_{\delta_q}}(\mathcal{M},\delta_q) \end{bmatrix}\right\} + mg\begin{bmatrix} -\sin\theta \\ 0 \\ \cos\theta \end{bmatrix} \tag{B1}$$

$$\begin{bmatrix} L \\ M \\ N \end{bmatrix} = \bar{q}Sd\left\{\begin{bmatrix} 0 \\ C_{m_S}(\mathcal{M},\alpha,\beta) \\ C_{n_S}(\mathcal{M},\alpha,\beta) \end{bmatrix} + \left(\frac{d}{2V}\right)\begin{bmatrix} C_{l_p}(\mathcal{M})p \\ C_{m_q}(\mathcal{M})q \\ C_{n_r}(\mathcal{M})r \end{bmatrix} + \begin{bmatrix} C_{l_{\delta_p}}(\mathcal{M},\delta_p) \\ C_{m_{\delta_q}}(\mathcal{M},\delta_q) \\ 0 \end{bmatrix}\right\} \tag{B2}$$

where S and d stand for the projectile's reference surface and caliber, θ represents the pitch angle, V is the airspeed, and $\bar{q}$ consists of the dynamic pressure.

The static models were obtained through an exhaustive regression analysis, based on a set of CFD campaigns. The regression analysis was performed with respect to the variation of the angle of attack α, the angle of sideslip β, and the Mach number $\mathcal{M}$. Two aerodynamic models of different complexity were developed. The first relies on a simple linear regression, which considers only the extreme configurations of the projectile dynamics, where the longitudinal and the lateral channels are assumed decoupled. Thus, either the effect of α or β is considered for each coefficient regression:

$$\begin{aligned}
C_{X_S}(\mathcal{M},\alpha) &= C_{X_{\alpha_0}}(\mathcal{M}) + C_{X_{\alpha^2}}(\mathcal{M})\sin^2\alpha + C_{X_{\alpha_4}}(\mathcal{M})\sin^4\alpha,\\
C_{Y_S}(\mathcal{M},\beta) &= C_{Y_{\beta_1}}(\mathcal{M})\sin\beta,\\
C_{Z_S}(\mathcal{M},\alpha) &= C_{Z_{\alpha_1}}(\mathcal{M})\sin\alpha,\\
C_{m_S}(\mathcal{M},\alpha) &= C_{m_{\alpha_1}}(\mathcal{M})\sin\alpha + C_{m_{\alpha_3}}(\mathcal{M})\sin^3\alpha + C_{m_{\alpha_5}}(\mathcal{M})\sin^5\alpha,\\
C_{n_S}(\mathcal{M},\beta) &= C_{n_{\beta_1}}(\mathcal{M})\sin\beta
\end{aligned} \tag{B3}$$

The second model is based on a multivariable regression, where the projectile longitudinal and lateral channels are coupled by the roll effect, and the simultaneous variations of α and β become relevant:

$$\begin{aligned}
C_{X_S}(\mathcal{M},\alpha,\beta) &= C_{X_0}(\mathcal{M}) + C_{X_2}(\mathcal{M})\cos\alpha\cos\beta\\
&\quad + C_{X_4}(\mathcal{M})\cos^2\alpha\cos^2\beta,\\
C_{Y_S}(\mathcal{M},\alpha,\beta) &= C_{Y_1}(\mathcal{M})\sin\beta + C_{Y_2}(\mathcal{M})\sin\beta\cos\beta\cos\alpha,\\
C_{Z_S}(\mathcal{M},\alpha,\beta) &= C_{Z_2}(\mathcal{M})\sin\alpha\cos\beta,\\
C_{m_S}(\mathcal{M},\alpha,\beta) &= C_{m_2}(\mathcal{M})\sin\alpha\cos\beta + C_{m_4}(\mathcal{M})\sin\alpha\cos\alpha\cos^2\beta,\\
C_{n_S}(\mathcal{M},\alpha,\beta) &= C_{n_1}(\mathcal{M})\sin\beta + C_{n_2}(\mathcal{M})\sin\beta\cos\beta\cos\alpha
\end{aligned} \tag{B4}$$

All the elementary coefficients (e.g., $C_{X_{\alpha_0}}$) represent the parameters identified during the regression analyses. Likewise, the aerodynamic control contributions were modeled through a regression analysis on a dedicated CFD data set, as a function of the Mach number, and the virtual control deflection angles δ_q, δ_p, and δ_{eff}:

$$\begin{aligned}
C_{X_{\delta_{\text{eff}}}}(\mathcal{M},\delta_{\text{eff}}) &= C_{X_{\delta_{\text{eff}_0}}}(\mathcal{M}) + C_{X_{\delta_{\text{eff}_2}}}(\mathcal{M})\sin^2\delta_{\text{eff}},\\
C_{Z_{\delta_q}}(\mathcal{M},\delta_q) &= C_{Z_{\delta_{q_1}}}(\mathcal{M})\sin\delta_q + C_{Z_{\delta_{q_3}}}(\mathcal{M})\sin^3\delta_q,\\
C_{l_{\delta_p}}(\mathcal{M},\delta_p) &= C_{l_{\delta_{p_1}}}(\mathcal{M})\sin\delta_p + C_{l_{\delta_{p_3}}}(\mathcal{M})\sin^3\delta_p,\\
C_{m_{\delta_q}}(\mathcal{M},\delta_q) &= C_{m_{\delta_{q_1}}}(\mathcal{M})\sin\delta_q + C_{m_{\delta_{q_3}}}(\mathcal{M})\sin^3\delta_q
\end{aligned} \tag{B5}$$

The *Simple Linear* static model in Eq. (B3) is employed for the autopilot design, together with a first-order linear approximation of the control coefficients in Eq. (B5) ($C_{X_{\delta_{\text{eff}}}}$ is completely neglected), whereas the complete *Multivariable* static model in Eq. (B4) is included in the simulator environment with the full control coefficients in Eq. (B5), for a more realistic testing purpose.

Appendix C: State Transformation Procedure

Assuming the output nonlinear model, expressed as a function of the time-varying parameters in $\rho(t)$, as:

$$\begin{bmatrix}\dot{\alpha}\\ \dot{q}\end{bmatrix}=\begin{bmatrix}f_1(\rho)\\ f_2(\rho)\end{bmatrix}+\begin{bmatrix}0 & A_{12}(\rho)\\ 0 & A_{22}(\rho)\end{bmatrix}\begin{bmatrix}\alpha\\ q\end{bmatrix}+\begin{bmatrix}B_1(\rho)\\ B_2(\rho)\end{bmatrix}\delta_q;$$
$$\rho(t)=[\alpha(t),V(t),h(t)] \tag{C1}$$

where:

$$A_{12}(\rho)=1+\frac{\bar{q}SdC_{Z_q}\cos\alpha}{2mV^2};\qquad B_1(\rho)=\frac{\bar{q}SC_{Z_{\delta_1}}\cos\alpha}{mV};$$
$$A_{22}(\rho)=\frac{\bar{q}Sd^2C_{m_q}}{2I_{yy}V};\qquad B_2(\rho)=\frac{\bar{q}SdC_{m_{\delta_1}}}{I_{yy}};$$
$$f_1(\rho)=-\frac{X\sin\alpha}{mV}+\frac{\bar{q}SC_{Z_s}\cos\alpha}{mV}+\frac{g}{V}\left(\sin\alpha\sin\bar{\theta}+\cos\alpha\cos\bar{\theta}\right);$$
$$f_2(\rho)=\frac{\bar{q}SdC_{m_s}}{I_{yy}}$$

by zeroing the dynamics associated with α, and q, it is possible to define the system trimming conditions as a function of $\rho(t)$ as follows:

$$\begin{cases}f_1(\rho)+A_{12}(\rho)q_{\text{eq}}+B_1(\rho)\delta_{q,\text{eq}}=0\\ f_2(\rho)+A_{22}(\rho)q_{\text{eq}}+B_2(\rho)\delta_{q,\text{eq}}=0\end{cases} \tag{C2}$$

The solution of the system of equations in Eq. (C2) leads to the parameter-varying equilibrium functions related to the pitch rate and to the input virtual deflection, respectively:

$$q_{\text{eq}}(\rho)=\frac{B_1(\rho)f_2(\rho)-B_2(\rho)f_1(\rho)}{A_{12}(\rho)B_2(\rho)-A_{22}(\rho)B_1(\rho)};$$
$$\delta_{q,\text{eq}}(\rho)=-\frac{A_{12}(\rho)f_2(\rho)-A_{22}(\rho)f_1(\rho)}{A_{12}(\rho)B_2(\rho)-A_{22}(\rho)B_1(\rho)}$$

Then, by subtracting the trimming conditions in Eq. (C2) from the nonlinear dynamics in Eq. (C1), the transformed model is obtained:

$$\begin{bmatrix}\dot{\alpha}\\ \dot{q}\end{bmatrix}=\begin{bmatrix}0 & A_{12}(\rho)\\ 0 & A_{22}(\rho)\end{bmatrix}\begin{bmatrix}\alpha\\ q_{\text{dev}}\end{bmatrix}+\begin{bmatrix}B_1(\rho)\\ B_2(\rho)\end{bmatrix}\delta_{q,\text{dev}} \tag{C3}$$

where the new off-equilibrium values of the pitch rate q_{dev} and virtual pitch deflection input $\delta_{q,\text{dev}}$ are defined by the transformation as:

$$q_{\text{dev}}:=q-q_{\text{eq}}(\rho);\qquad \delta_{q,\text{dev}}:=\delta_q-\delta_{q,\text{eq}}(\rho) \tag{C4}$$

The dynamics of the off-equilibrium state q_{dev} is expressed through the partial derivatives of the corresponding equilibrium function $q_{\text{eq}}(\rho)$ as:

$$\dot{q}_{\text{dev}}:=\dot{q}-\dot{q}_{\text{eq}}; \tag{C5}$$

with:

$$\dot{q}_{\text{eq}}=\frac{dq_{\text{eq}}}{dt}=\frac{\partial q_{\text{eq}}}{\partial\alpha}\dot{\alpha}+\frac{\partial q_{\text{eq}}}{\partial V}\dot{V}+\frac{\partial q_{\text{eq}}}{\partial h}\dot{h} \tag{C6}$$

The partial derivatives related to the exogenous scheduling variables V and h are neglected, in reason of the very limited impact they have on the off-equilibrium dynamics. They are generally assumed as external sources of disturbance to be compensated during the control design stage [15,17].

By substituting the dynamics of α, defined in Eq. (C3), into the approximated version of Eq. (C6), the following expression is obtained:

$$\dot{q}_{\text{eq}}\approx\frac{\partial q_{\text{eq}}}{\partial\alpha}\dot{\alpha}=\frac{\partial q_{\text{eq}}}{\partial\alpha}\left(A_{12}q_{\text{dev}}+B_1\delta_{q,\text{dev}}\right) \tag{C7}$$

As a result, by considering the dynamics of q in Eq. (C3) and the equilibrium dynamics in Eq. (C8), the off-equilibrium dynamics defined in Eq. (C5) can be expressed as:

$$\dot{q}_{\text{dev}}=\left(A_{22}-\frac{\partial q_{\text{eq}}}{\partial\alpha}A_{12}\right)q_{\text{dev}}+\left(B_2-\frac{\partial q_{\text{eq}}}{\partial\alpha}B_1\right)\delta_{q,\text{dev}} \tag{C8}$$

Thus, the (state transformed) quasi-LPV version of the original nonlinear model in Eq. (C1) corresponds to:

$$\begin{bmatrix}\dot{\alpha}\\ \dot{q}_{\text{dev}}\end{bmatrix}=\begin{bmatrix}0 & A_{12}(\rho)\\ 0 & A_{22}-\frac{\partial q_{\text{eq}}}{\partial\alpha}A_{12}\end{bmatrix}\begin{bmatrix}\alpha\\ q_{\text{dev}}\end{bmatrix}+\begin{bmatrix}B_1(\rho)\\ B_2-\frac{\partial q_{\text{eq}}}{\partial\alpha}B_1\end{bmatrix}\delta_{q,\text{dev}}$$

However, the obtained quasi-LPV model is expressed with respect to the off-equilibrium input $\delta_{q,\text{dev}}$ and, consequently, as a function of the trimming condition $\delta_{q,\text{eq}}$ that has to be continuously updated. In terms of system stability and robustness, this internal feedback loop might be critical. A straightforward solution consists of restricting the validity of the formulation to those flight conditions where $\delta_{q,\text{eq}}=0$. Nevertheless, this imposition represents a strong limitation to the operating flight envelope of the projectile quasi-LPV model.

A standard alternative solution consists of augmenting an integrator at the plant input [1,15], defining:

$$\delta_q=\int\sigma$$

In this way, the new input σ is uniformly zero at every equilibrium point, and the internal feedback loop does not affect the system dynamics anymore.

By repeating the same procedure as in Eqs. (C5–C8) for the off-equilibrium input dynamics $\delta_{q,\text{dev}}$, defined in Eq. (C4), the final integrator-augmented quasi-LPV system is obtained:

$$\begin{bmatrix}\dot{\alpha}\\ \dot{q}_{\text{dev}}\\ \dot{\delta}_{q,\text{dev}}\end{bmatrix}=\begin{bmatrix}0 & A_{12}(\rho) & B_1(\rho)\\ 0 & A_{22}(\rho)-\frac{\partial q_{\text{eq}}}{\partial\alpha}A_{12}(\rho) & B_2(\rho)-\frac{\partial q_{\text{eq}}}{\partial\alpha}B_1(\rho)\\ 0 & -\frac{\partial\delta_{q,\text{eq}}}{\partial\alpha}A_{12}(\rho) & -\frac{\partial\delta_{q,\text{eq}}}{\partial\alpha}B_1(\rho)\end{bmatrix}\times\begin{bmatrix}\alpha\\ q_{\text{dev}}\\ \delta_{q,\text{dev}}\end{bmatrix}+\begin{bmatrix}0\\ 0\\ 1\end{bmatrix}\sigma$$

References

[1] Shamma, J. S., and Cloutier, J. R., "Gain-Scheduled Missile Autopilot Design Using Linear Parameter Varying Transformations," *Journal of Guidance, Control, and Dynamics*, Vol. 16, No. 2, 1993, pp. 256–263. https://doi.org/10.2514/3.20997

[2] Carter, L. H., and Shamma, J. S., "Gain-Scheduled Bank-to-Turn Autopilot Design Using Linear Parameter Varying Transformations," *Journal of Guidance, Control, and Dynamics*, Vol. 19, No. 5, 1996, pp. 1056–1063. https://doi.org/10.2514/3.21745

[3] Prempain, E., Postlethwaite, I., and Vorley, D., "A Gain Scheduled Autopilot Design for a Bank-to-Turn Missile," *Proceedings of the 2001 European Control Conference (ECC)*, Inst. of Electrical and Electronics Engineers, New York, 2001, pp. 2052–2057. https://doi.org/10.23919/ECC.2001.7076224

[4] Theodoulis, S., and Proff, M., "Robust Flight Control Tuning for Highly Agile Missiles," *AIAA Scitech 2021 Forum*, AIAA Paper 2021-1568, 2021.
https://doi.org/10.2514/6.2021-1568

[5] Tan, W., Packard, A. K., and Balas, G. J., "Quasi-LPV Modeling and LPV Control of a Generic Missile," *Proceedings of the 2000 American Control Conference. ACC (IEEE Cat)*, Vol. 5, Inst. of Electrical and Electronics Engineers, New York, 2000, pp. 3692–3696.
https://doi.org/10.1109/ACC.2000.879259

[6] Balas, G. J., Fialho, I., Packard, A., Renfrow, J., and Mullaney, C., "On the Design of LPV Controllers for the F-14 Aircraft Lateral-Directional Axis During Powered Approach," *Proceedings of the 1997 American Control Conference (Cat. No. 97CH36041)*, Vol. 1, Inst. of Electrical and Electronics Engineers, New York, 1997, pp. 123–127.
https://doi.org/10.1109/ACC.1997.611768

[7] Yue, T., Wang, L., and Ai, J., "Gain Self-Scheduled H_∞ Control for Morphing Aircraft in the Wing Transition Process Based on an LPV Model," *Chinese Journal of Aeronautics*, Vol. 26, No. 4, 2013, pp. 909–917.
https://doi.org/10.1016/j.cja.2013.06.004

[8] Hjartarson, A., Seiler, P., and Balas, G. J., "LPV Analysis of a Gain Scheduled Control for an Aeroelastic Aircraft," *American Control Conference*, Inst. of Electrical and Electronics Engineers, New York, 2014, pp. 3778–3783.
https://doi.org/10.1109/ACC.2014.6859301

[9] Sève, F., Theodoulis, S., Wernert, P., Zasadzinski, M., and Boutayeb, M., "Pitch/Yaw Channels Control Design for a 155 mm Projectile with Rotating Canards, Using a H_∞ Loop-Shaping Design Procedure," *AIAA Guidance, Navigation, and Control Conference*, AIAA Paper 2014-1474, 2014.
https://doi.org/10.2514/6.2014-1474

[10] Theodoulis, S., Gassmann, V., Wernert, P., Dritsas, L., Kitsios, I., and Tzes, A., "Guidance and Control Design for a Class of Spin-Stabilized Fin-Controlled Projectiles," *Journal of Guidance, Control, and Dynamics*, Vol. 36, No. 2, 2013, pp. 517–531.
https://doi.org/10.2514/1.56520

[11] Theodoulis, S., Sève, F., and Wernert, P., "Robust Gain-Scheduled Autopilot Design for Spin-Stabilized Projectiles with a Course-Correction Fuze," *Aerospace Science and Technology*, Vol. 42, April–May 2015, pp. 477–489.
https://doi.org/10.1016/j.ast.2014.12.027

[12] Strub, G., Theodoulis, S., Gassmann, V., Dobre, S., and Basset, M., "Gain-Scheduled Autopilot Design and Validation for an Experimental Guided Projectile Prototype," *Journal of Guidance, Control, and Dynamics*, Vol. 41, No. 2, 2018, pp. 461–475.
https://doi.org/10.2514/1.G002916

[13] Sève, F., and Theodoulis, S., "Design of an H_∞ Gain-Scheduled Guidance Scheme for a Guided Projectile," *Journal of Guidance, Control, and Dynamics*, Vol. 42, No. 11, 2019, pp. 2399–2417.
https://doi.org/10.2514/1.G004317

[14] Shamma, J. S., and Athans, M., "Gain Scheduling: Potential Hazards and Possible Remedies," *IEEE Control Systems Magazine*, Vol. 12, No. 3, 1992, pp. 101–107.
https://doi.org/10.1109/37.165527

[15] Leith, D. J., and Leithead, W. E., "Survey of Gain-Scheduling Analysis and Design," *International Journal of Control*, Vol. 73, No. 11, 2000, pp. 1001–1025.
https://doi.org/10.1080/002071700411304

[16] Marcos, A., and Balas, G. J., "Development of Linear-Parameter-Varying Models for Aircraft," *Journal of Guidance, Control, and Dynamics*, Vol. 27, No. 2, 2004, pp. 218–228.
https://doi.org/10.2514/1.9165

[17] Balas, G. J., "Linear, Parameter-Varying Control and Its Application to Aerospace Systems," *Proceedings of the 23rd International Congress of Aeronautical Sciences*, International Council of the Aeronautical Sciences (ICAS), Toronto, Canada, 2002, https://www.icas.org/ICAS_ARCHIVE/ICAS2002/ABSTRACTS/541.HTM.

[18] Poussot-Vassal, C., and Roos, C., "Generation of a Reduced-Order LPV/LFT Model from a Set of Large-Scale MIMO LTI Flexible Aircraft Models," *Control Engineering Practice*, Vol. 20, No. 9, 2012, pp. 919–930.
https://doi.org/10.1016/j.conengprac.2012.06.001

[19] Wu, F., Packard, A., and Balas, G., "LPV Control Design for Pitch-Axis Missile Autopilots," *Proceedings of 1995 34th IEEE Conference on Decision and Control*, Vol. 1, Inst. of Electrical and Electronics Engineers, New York, 1995, pp. 188–193.
https://doi.org/10.1109/CDC.1995.478672

[20] Pfifer, H., and Hecker, S., "LPV Controller Synthesis for a Generic Missile Model," *2010 IEEE International Conference on Control Applications*, Inst. of Electrical and Electronics Engineers, New York, 2010, pp. 1838–1843.
https://doi.org/10.1109/CCA.2010.5611127

[21] Pfifer, H., and Hecker, S., "Generation of Optimal Linear Parametric Models for LFT-Based Robust Stability Analysis and Control Design," *IEEE Transactions on Control Systems Technology*, Vol. 19, No. 1, 2010, pp. 118–131.
https://doi.org/10.1109/TCST.2010.2076329

[22] Pellanda, P. C., Apkarian, P., and Tuan, H. D., "Missile Autopilot Design ia a Multi-Channel LFT/LPV Control Method," *International Journal of Robust and Nonlinear Control*, Vol. 12, No. 1, 2002, pp. 1–20.
https://doi.org/10.1002/(ISSN)1099-1239

[23] Bryson, J., and Gruenwald, B. C., "Linear Parameter Varying Model Predictive Control of a High-Speed Projectile," *AIAA Scitech 2022 Forum*, AIAA Paper 2022-1585, 2022.
https://doi.org/10.2514/6.2022-1585

[24] Apkarian, P., Gahinet, P., and Becker, G., "Self-Scheduled H_∞ Control of Linear Parameter-Varying Systems: A Design Example," *Automatica*, Vol. 31, No. 9, 1995, pp. 1251–1261.
https://doi.org/10.1016/0005-1098(95)00038-X

[25] Jin, X., Yin, G., Zeng, X., and Chen, J., "Robust Gain-Scheduled Output Feedback Yaw Stability Control for In-Wheel-Motor-Driven Electric Vehicles with External Yaw-Moment," *Journal of the Franklin Institute*, Vol. 355, No. 18, 2018, pp. 9271–9297.
https://doi.org/10.1016/j.jfranklin.2017.07.006

[26] Kapsalis, D., Sename, O., Milanes, V., and Molina, J. J., "A Reduced LPV Polytopic Look-Ahead Steering Controller for Autonomous Vehicles," *Control Engineering Practice*, Vol. 129, Dec. 2022, Paper 105360.
https://doi.org/10.1016/j.conengprac.2022.105360

[27] Zhang, H., Zhang, X., and Wang, J., "Robust Gain-Scheduling Energy-to-Peak Control of Vehicle Lateral Dynamics Stabilisation," *Vehicle System Dynamics*, Vol. 52, No. 3, 2014, pp. 309–340.
https://doi.org/10.1080/00423114.2013.879190

[28] Corno, M., Panzani, G., Roselli, F., Giorelli, M., Azzolini, D., and Savaresi, S. M., "An LPV Approach to Autonomous Vehicle Path Tracking in the Presence of Steering Actuation Nonlinearities," *IEEE Transactions on Control Systems Technology*, Vol. 29, No. 4, 2020, pp. 1766–1774.
https://doi.org/10.1109/TCST.2020.3006123

[29] Palladino, L., Duc, G., and Pothin, R., "LPV Control for μ-Split Braking Assistance of a Road Vehicle," *Proceedings of the 44th IEEE Conference on Decision and Control*, Inst. of Electrical and Electronics Engineers, New York, 2005, pp. 2664–2669.
https://doi.org/10.1109/CDC.2005.1582565

[30] Panshuo, L., Anh-Tu, N., Haiping, D., Yan, W., and Hui, Z., "Polytopic LPV Approaches for Intelligent Automotive Systems: State of the Art and Future Challenges," *Mechanical Systems and Signal Processing*, Vol. 161, Dec. 2021, Paper 107931.
https://doi.org/10.1016/j.ymssp.2021.107931

[31] Hoffmann, C., and Werner, H., "A Survey of Linear Parameter-Varying Control Applications Validated by Experiments or High-Fidelity Simulations," *IEEE Transactions on Control Systems Technology*, Vol. 23, No. 2, 2015, pp. 416–433.
https://doi.org/10.1109/TCST.2014.2327584

[32] Kwiatkowski, A., and Werner, H., "PCA-Based Parameter Set Mappings for LPV Models with Fewer Parameters and Less Overbounding," *IEEE Transactions on Control Systems Technology*, Vol. 16, No. 4, 2008, pp. 781–788.
https://doi.org/10.1109/TCST.2007.903094

[33] Fresconi, F., "Guidance and Control of a Projectile with Reduced Sensor and Actuator Requirements," *Journal of Guidance, Control, and Dynamics*, Vol. 34, No. 6, 2011, pp. 1757–1766.
https://doi.org/10.2514/1.53584

[34] Cooper, G., Fresconi, F., and Costello, M., "Flight Stability of an Asymmetric Projectile with Activating Canards," *Journal of Spacecraft and Rockets*, Vol. 49, No. 1, 2012, pp. 130–135.
https://doi.org/10.2514/1.A32022

[35] Vasile, J. D., Bryson, J., Gruenwald, B. C., Fairfax, L., Strohm, L., and Fresconi, F., "A Multi-Disciplinary Approach to Design Long Range Guided Projectiles," *AIAA Scitech 2020 Forum*, AIAA Paper 2020-1993, 2020.
https://doi.org/10.2514/6.2020-1993

[36] Vinco, G. M., Theodoulis, S., and Sename, O., "Flight Dynamics Modeling and Simulator Design for a New Class of Long-Range Guided Projectiles," *Proceedings of the 2022 CEAS EuroGNC Conference*, CEAS Paper GNC-2022-034, 2022, https://hal.univ-grenoble-alpes.fr/hal-03654390, https://eurognc.ceas.org/archive/EuroGNC2022/html/CEAS-GNC-2022-034.html.

[37] Vinco, G. M., Theodoulis, S., Sename, O., and Strub, G., "Quasi-LPV Modeling of Guided Projectile Pitch Dynamics Through State Transformation Technique," *IFAC-PapersOnLine*, Vol. 55, No. 35, 2022, pp. 43–48.
https://doi.org/10.1016/j.ifacol.2022.11.288

[38] Phillips, C. A., "Guidance Algorithm for Range Maximization and Time-of-Flight Control of a Guided Projectile," *Journal of Guidance, Control, and Dynamics*, Vol. 31, No. 5, 2008, pp. 1447–1455.
https://doi.org/10.2514/1.31327

[39] Kelley, H. J., Cliff, E. M., and Lutze, F. H., "Boost–Glide Range-Optimal Guidance," *Optimal Control Applications and Methods*, Vol. 3, No. 3, 1982, pp. 293–298.
https://doi.org/10.1002/oca.4660030307

[40] *Standard Atmosphere*, 1st ed., International Organization for Standardization, May 1975, p. 108, https://www.iso.org/standard/7472.html.

[41] Zipfel, P. H., *Modeling and Simulation of Aerospace Vehicle Dynamics*, 3rd ed., AIAA, Reston, VA, 2014, pp. 17–54, 97–236, 411–460, Chaps. 2, 4–6, 10.
https://doi.org/10.2514/4.102509